CHALMERS
UNIVERSITY OF TECHNOLOGY

CELL ELECTROPERMEABILIZATION MODELING VIA MULTIPLE TRACES FORMULATION AND TIME SEMI-IMPLICIT MULTISTEP

SIAM J. SCI. COMPUT.
Vol. 46, No. 6, pp. B953–B980

CELL ELECTROPERMEABILIZATION MODELING VIA MULTIPLE TRACES FORMULATION AND TIME SEMI-IMPLICIT MULTISTEP COUPLING*

ISABEL A. MARTÍNEZ ÁVILA†, CARLOS JEREZ-HANCKES‡, AND IRINA PETTERSSON§

Abstract. We simulate the electrical response of multiple disjoint biological three-dimensional cells undergoing an electropermeabilization process. Instead of solving the boundary value problem in the unbounded volume, we reduce it to a system of boundary integrals equations—the local multiple traces formulation—coupled with nonlinear dynamics on the cell membranes. Though in time the model is highly nonlinear and poorly regular, the smooth geometry allows for boundary unknowns to be spatially approximated by spherical harmonics. This leads to spectral convergence rates in space. In time, we use a multistep semi-implicit scheme. To ensure stability, the time step needs to be bounded by the smallest characteristic time of the system. Numerical results are provided to validate our claims, and future enhancements are pointed out.

Key words. electropermeabilization, semi-implicit scheme, boundary integral equations, multiple traces formulation, transmembrane potential, multistep methods

MSC codes. 65R20, 92C37, 65M70, 65J15

DOI. 10.1137/23M1570260

1. Introduction.

Electropermeabilization designates the use of short high voltage or electric field pulses to increase the permeability of the cell membrane and its potential to allow the access of nonpermeant molecules [19, 26]. This technique is used to deliver therapeutic molecules such as drugs and genes into cells to treat cancer, perform genetic engineering, and screen drugs, among others applications (cf. [18]).

Theoretically, several models have been proposed to describe the reversible membrane electropermeabilization mechanism without rigorous proof. For instance, during electropermeabilization it is thought that aqueous pores are formed along the cell membrane—electroporation—thereby increasing the permeability of the membrane. Yet, this has not been experimentally observed to occur for voltages used in practice. The pores are either too small to be seen by optical microscopy or too fragile for electron imaging. Only molecular dynamics' simulations have been able to demonstrate pore formation (cf. [19, section 3], [3, section 2.1]). Moreover, the application of external electric pulses triggers other physical and chemical cell mechanisms, many of them not fully understood due to the complex interactions at multiple length scales: from nanometers at the cell membrane to centimeters in tissues [19]. "*Therefore, while the term electroporation is commonly used among biologists, the term electroperme-*

*Submitted to the journal's Software, High-Performance Computing, and Computational Science and Engineering section May 2, 2023; accepted for publication (in revised form) August 23, 2024; published electronically December 17, 2024.

https://doi.org/10.1137/23M1570260

Funding: This work was funded by the Agencia Nacional de Investigación y Desarrollo (ANID), through the doctoral fellowship program Conicyt-PFCHA/Doctorado Nacional/2018-21181809 and Fondecyt Regular 1231112. This work was supported by Swedish Foundation for International Cooperation in Research and Higher education (STINT) CS2018-7908.

†Computational Biology Lab, Fundacion Ciencia Para la Vida, Universidad San Sebastian, Santiago, Chile (iamartinez@dlab.cl).

‡Facultad de Ingeniería y Ciencias, Universidad Adolfo Ibáñez, Santiago, Chile (carlos.jerez@uai.cl).

§Chalmers University of Technology and Gothenburg University, Gothenburg, Sweden (irinap@chalmers.se).

abilization should be preferred in order to prevent any molecular description of the phenomenon" [26].

Still, mathematical models and numerical methods can lead to a better understanding of the different underlying phenomena. For instance, Neu and Krassowska [23] consider a pure electroporation process by modeling the nanoscale phenomena involved in the creation and resealing of the cell membrane pores, and they apply homogenization theory to derive nonlinear-in-time dynamics. Well-posedness of the Neu–Krassowska model and a new one including anisotropies are derived in [2]. Alternatively, in [17] the authors propose a phenomenological model that forgoes the ab initio understanding of the mechanisms involved. A more complete phenomenological model splits the electroporation process into two different stages: conducting and permeable [20]. This model also takes into account the diffusion and electric transport of nonpermeable molecules. In [10, 22], the authors discard particle diffusion and transport in [20] to then apply the Voronoi Interface Method [9] for its numerical approximation. Specifically, they construct a Voronoi mesh of the volume coupled to a ghost fluid method to capture discontinuous boundary conditions. Further computational enhancements via parallelization are given in [22].

Instead of solving the volume boundary value problem, we recast the problem onto cell membranes via the local multiple traces formulation (MTF) [13, 4, 14, 5, 16]. Originally introduced to solve acoustic wave transmission problems in heterogeneous scatterers, the local MTF considers independent trace unknowns at either side of the subdomains' boundaries to then enforce continuity conditions weakly via Calderón identities. In [12, 11] the method was successfully applied to model the electrical behavior of peripheral neurons by coupling the Laplace boundary integral operators with Hodgkin–Huxley nonlinear dynamics. The volume Laplace equations in intra- and extracellular media arise when assuming a quasi-static electromagnetic regime, and one can show that for two and three dimensions the model is well-posed. Numerically, the authors prove stability and convergence of the multistep semi-implicit time discretizations with low- and high- (spectral) order spatial boundary unknown representations. Moreover, the numerical method proposed can be extended to model other nonlinear dynamics.

Following [12, 11], we employ the above boundary integral equations to simulate the electric potential response of multiple disjoint cells in three dimensions when subject to electric pulses. Spatially, the boundary unknowns will be approximated by spherical harmonics, thereby allowing for spectral convergence rates in space. The nonlinear dynamics of the cell membrane follow [17] and are solved by a multistep semi-implicit scheme. As we will see, the dynamic model is in fact highly nonlinear and portrays poor regularity, reason for which convergence rates in time are low when compared to spatial ones.

The rest of the paper is organized as follows. In section 2 we formulate the problem and the corresponding nonlinear dynamic model, and derive MTF. In section 3, we present a numerical scheme for spatial and time-domain discretizations, as well as discuss advantages and limitations of the proposed method. Computational results are provided in section 4. Code validation experiments with analytic and overkill solutions confirm our theoretical results and open new avenues of research.

2. Problem statement and boundary integral formulation.

2.1. Dirichlet and Neumann traces. In what follows we will need the notion of Dirichlet and Neumann traces, which we introduce below. Let $\Omega \subset \mathbb{R}^d$, $d = 1, 2, 3$,

be an open nonempty domain not necessarily bounded with a Lipschitz boundary Γ. For $u \in C^\infty(\overline{\Omega})$, Dirichlet and Neumann traces operators are defined as

$$\gamma_D u := u|_\Gamma, \qquad \gamma_N u := (\nabla u \cdot \widehat{\mathbf{n}})\,|_\Gamma,$$

where $\widehat{\mathbf{n}}$ is the exterior unit normal and ∇ denotes the gradient. For a Lipschitz Γ, the Dirichlet trace has a unique extension to a linear and continuous operator $\gamma_D : H^1_{loc}(\Omega) \to H^{1/2}(\Gamma)$, where[1]

$$\|v\|_{H^{\frac{1}{2}}(\Gamma)} := \left\{ \inf_{u \in H^1(\Omega)} \|u\|_{H^1(\Omega)} :\ \gamma_D u = v \right\}.$$

The space of bounded linear functionals on $H^{\frac{1}{2}}(\Gamma)$ is denoted by $H^{-\frac{1}{2}}(\Gamma)$. Let Δ denote the Laplace operator, and define

$$H^1_{loc}(\Delta, \Omega) := \left\{ u \in H^1_{loc}(\Delta, \Omega) \ :\ \Delta u \in L^2_{loc}(\Omega) \right\}.$$

One can also show that the Neumann trace operator $\gamma_N : H^1_{loc}(\Delta, \Omega) \to H^{-\frac{1}{2}}(\Gamma)$ is continuous (see [27, sections 2.6–2.8]). $H^{\frac{1}{2}}(\Gamma)$ and $H^{-\frac{1}{2}}(\Gamma)$ are referred to as Dirichlet and Neumann trace spaces, respectively [27, sections 2.4, 2.6, and 2.7].

2.2. Cell electropermeabilization model. We now present a continuous model used for the electropermeabilization process. Specifically, we assume a quasi-static electromagnetic problem in the intra- and extracellular domains coupled with nonlinear dynamics at the cells' membranes. This coupling relies on enforcing adequate transmission conditions for potentials and currents across the cells. By a quasi-static regime, we imply that the frequency of the electric fields is low enough to discard any time delay in electromagnetic wave propagation [25].

We consider the electric interaction of $\mathcal{N} \in \mathbb{N}$ disjoint spherical cells located at $\mathbf{p_j} \in \mathbb{R}^3$ with radii $R_j \in \mathbb{R}^+$, $j \in \{1, \ldots, \mathcal{N}\}$. We define the interior space of the jth cell by $\Omega_j := \{\mathbf{x} \in \mathbb{R}^3 : \|\mathbf{x} - \mathbf{p_j}\|_2 < R_j\}$, with its membrane being the boundary $\Gamma_j := \partial\Omega_j = \{\mathbf{x} \in \mathbb{R}^3 : \|\mathbf{x} - \mathbf{p_j}\|_2 = R_j\}$. The extracellular medium is defined as the complement to the intracellular domain: $\Omega_0 := \mathbb{R}^3 \setminus \bigcup_{j=1}^{\mathcal{N}} \overline{\Omega}_j$. An illustration for three cells is presented in Figure 1.

For $j \in \{0, \ldots, N\}$, each cell Ω_j is assumed to have constant conductivity $\sigma_j \in \mathbb{R}^+$. For $T \in \mathbb{R}^+$, let $\phi_e : [0, T] \times \Omega_0 \to \mathbb{R}$ be a given external potential. Let $u_0 : [0, T] \times \Omega_0 \to \mathbb{R}$ be the electric potential without excitation in the extracellular medium, so that the

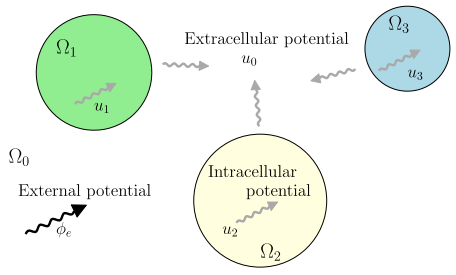

FIG. 1. *A system of three cells* $\mathcal{N} = 3$.

[1]We use the subscript *loc* for locally integrable spaces, in particular, when Ω is unbounded (cf. [21]).

total external potential is $u_0^{tot} := u_0 + \phi_e$. We denote by $u_j : [0,T] \times \Omega_j \to \mathbb{R}$, $j \in \{1,\dots,\mathcal{N}\}$, the electric potential inside the jth cell, as in Figure 1.

Across cell membranes Γ_j the potential is discontinuous, the difference $v_j := u_j - u_0$ is called the *membrane or transmembrane* potential, and the flux is assumed to be continuous. Thus, our boundary value problem becomes[2]

$$\begin{aligned} \operatorname{div}(\sigma_j \nabla u_j) &= 0, && (t,\mathbf{x}) \in [0,T] \times \Omega_j,\ j \in \{0,\dots,\mathcal{N}\}, \\ -\gamma_D^{0j} u_0 + \gamma_D^j u_j &= v_j + \gamma_D^{0j} \phi_e, && (t,\mathbf{x}) \in [0,T] \times \Gamma_j,\ j \in \{1,\dots,\mathcal{N}\}, \\ \sigma_0 \gamma_N^{0j} u_0 + \sigma_j \gamma_N^j u_j &= -\sigma_0 \gamma_N^{0j} \phi_e, && (t,\mathbf{x}) \in [0,T] \times \Gamma_j,\ j \in \{1,\dots,\mathcal{N}\}. \end{aligned}$$

Observe that Neumann jumps consider the inherited normal outward direction for each subdomain, so that $\gamma_N^{0j} = -\gamma_N^j$.

For the electropermeabilization process, we adopt the phenomenological model presented in [17]. Specifically, at each cell $j \in \{1,\dots,\mathcal{N}\}$, one has

$$\begin{aligned} c_{m,j} \partial_t v_j + I_j^{ep}(v_j, Z_j) &= -\sigma_j \gamma_N^j u_j && \text{on } [0,T] \times \Gamma_j, \\ I_j^{ep}(v_j, Z_j) &= v_j (S_{L,j} + Z_j(t, v_j(t,\mathbf{x}))(S_{ir,j} - S_{L,j})) && \text{on } [0,T] \times \Gamma_j, \end{aligned}$$

with $c_{m,j}$ denoting the membrane capacitance per unit area, and I_j^{ep} being the electropermeabilization current. This last quantity depends on the transmembrane potential v_j and a C^1-function $Z_j : [0,T] \times \Gamma_j \to [0,1]$ (cf. [17, Lemma 7]). For brevity, and slightly abusing the notation, we write $Z_j(t,\mathbf{x})$ instead of $Z_j(t, v_j(t,\mathbf{x}))$. The variable $Z_j(t,\mathbf{x})$ "*measures in some way the likelihood that a given infinitesimal portion of the membrane is going to be electropermeabilized*" [17, p. 247]. Specifically, Z_j enforces the surface membrane conductivity to take values between two parameters: the surface conductivity $S_{ir,j}$ for which the electropermeabilization process becomes irreversible, and the lipid surface conductivity $S_{L,j}$. Indeed, when $Z_j = 0$, the membrane conductivity equals the lipid conductivity, and there is no electropermeabilization; if $Z_j = 1$, the membrane conductivity takes the maximal value above which electropermeabilization is irreversible. Following [17], Z_j satisfies the ordinary differential equation:[3]

$$\partial_t Z_j(t,\lambda) = \max\left(\frac{\beta_j(\lambda) - Z_j(t,\lambda)}{\tau_{ep,j}}, \frac{\beta_j(\lambda) - Z_j(t,\lambda)}{\tau_{res,j}} \right).$$

Here, $\beta_j \in W^{1,\infty}(\mathbb{R};[0,1]) := \{u \in L^\infty(\mathbb{R};[0,1]) : D^\alpha u \in L^\infty(\mathbb{R};[0,1]), |\alpha| \le 1\}$. If $\beta_j(v_j) - Z_j(t,v_j)$ is positive, the electric pulse is sufficiently intense to enlarge the electropermeabilized region with a characteristic time $\tau_{ep,j}$. Contrarily, if $\beta_j(v_j) - Z_j(t,v_j)$ is negative, the pulse is not strong enough to allow electropermeabilization and the membrane returns to its resting state, with a characteristic resealing time $\tau_{res,j}$. Experimental observations suggest that $\tau_{res,j} \gg \tau_{ep,j}$.

Remark 2.1. In general [17], one can use any function β_j such that $\beta_j \in W^{1,\infty}(\mathbb{R})$, $v\beta_j'(v) \in L^\infty(\mathbb{R})$, β_j is nondecreasing in $(0,\infty)$, $0 \le \beta_j(v) \le 1$, $\lim_{v\to\infty} \beta_j(v) = 1$. In our case, we set β_j as

$$\beta_j(v) := \frac{1 + \tanh(k_{ep,j}(|v| - V_{rev,j}))}{2}, \tag{2.1}$$

[2]Observe that the Dirichlet and Neumann operators only act in the spatial variable $\mathbf{x}$. For a collection of spheres, we have added superindices to emphasize where the traces are taken from, i.e., $0j$ for the traces arising from Ω_0 onto Γ_j, and j for the ones from Ω_j to Γ_j.

[3]One can see that functions Z_j will portray poor regularity—at most C^1—a fact later observed numerically.

wherein two additional parameters are introduced: the electropermeabilization switch speed $k_{ep,j}$ between $S_{ir,j}$ and $S_{L,j}$, and $V_{rev,j}$, the transmembrane potential threshold for electropermeabilization to occur. The chosen β_j (2.1) satisfies the above conditions. This can be checked by recalling the properties of the hyperbolic functions $\tanh : \mathbb{R} \to [-1,1]$ and $\operatorname{sech} : \mathbb{R} \to [0,1]$. We will assume that the threshold potential V_{rev} is constant throughout the electropermeabilization process.

In summary, the full electropermeabilization dynamic problem reads as follows.

PROBLEM 2.2. *Given $T \in \mathbb{R}^+$, an external potential $\phi_e \in C([0,T], H^1_{loc}(\Omega_0))$, and the initial conditions $u_j^0 \in H^1(\Omega_j)$ and $Z_j^0 \in H^{\frac{1}{2}}(\Gamma_j)$ for $j = 1, \dots, \mathcal{N}$, we seek $u_j \in C([0,T], H^1(\Omega_j))$, $v_j \in C([0,T], H^{\frac{1}{2}}(\Gamma_j))$, and $Z_j \in C([0,T], H^{\frac{1}{2}}(\Gamma_j))$ for $j \in \{1, \dots, \mathcal{N}\}$ such that for $t \in [0,T]$, the following holds:*

$$\operatorname{div}(\sigma_0 \nabla u_0) = 0 \qquad \text{in } \Omega_0, \tag{2.2a}$$

$$\operatorname{div}(\sigma_j \nabla u_j) = 0 \qquad \text{in } \Omega_j, \tag{2.2b}$$

$$-\gamma_D^{0j} u_0 + \gamma_D^j u_j = v_j + \gamma_D^{0j} \phi_e \qquad \text{on } \Gamma_j, \tag{2.2c}$$

$$\sigma_0 \gamma_N^{0j} u_0 + \sigma_j \gamma_N^j u_j = -\sigma_0 \gamma_N^{0j} \phi_e \qquad \text{on } \Gamma_j, \tag{2.2d}$$

$$c_{m,j} \partial_t v_j + I_j^{ep}(v_j, Z_j) = -\sigma_j \gamma_N^j u_j \qquad \text{on } \Gamma_j, \tag{2.2e}$$

$$u_j(0, \mathbf{x}) = u_j^0,\ Z_j(0, \mathbf{x}) = Z_j^0 \qquad \text{in } \Omega_j, \tag{2.2f}$$

$$u_0(0, \mathbf{x}) = u_0^0 \qquad \text{in } \Omega_0, \tag{2.2g}$$

$$u_0 = \mathcal{O}(\|\mathbf{x}\|_2^{-1}) \qquad \text{as } \|\mathbf{x}\|_2 \to \infty, \tag{2.2h}$$

with I_j^{ep} defined as

$$I_j^{ep}(v_j, Z_j) := v_j \left(S_{L,j} + Z_j(t, v_j)(S_{ir,j} - S_{L,j}) \right), \tag{2.3}$$

where the $Z_j(t, \lambda)$ satisfy

$$\partial_t Z_j(t, \lambda) = \max\left(\frac{\beta_j(\lambda) - Z_j(t,\lambda)}{\tau_{ep,j}}, \frac{\beta_j(\lambda) - Z_j(t,\lambda)}{\tau_{res,j}} \right) \tag{2.4}$$

with β_j given by (2.1) *and parameters $\tau_{ep,j}, \tau_{res,j}$ described above.*

As above, we write $Z_j(x, \mathbf{x}) = Z_j(t, v_j(t, \mathbf{x}))$. Observe that (2.2h) is the standard decay condition for the Laplace problem in three dimensions that guarantees that the problem is well-posed. Finally, the parameters of each cell $c_{m,j}$, $V_{ep,j}$, $\tau_{ep,j}$, and $\tau_{res,j}$ might differ from cell to cell. In practical applications, these parameters depend on the cell type, e.g., cancer cells possess material properties different from healthy cells in the same tissue [24].

2.3. Boundary integral formulation. Due to the unboundedness of the domain as well as the constant conductivity values inside intra- and extracellular domains, one can write Problem 2.2 using boundary integral operators, thereby reducing the volume problem to a boundary one as in [13, 12, 11]. Moreover, this significantly reduces the degrees of freedom required to solve the problem.

2.3.1. Boundary integral potential and operators. The free space fundamental solution of the Laplace equation for a source located at $\mathbf{x}'$ satisfying the decay condition (2.2h) is [15, section 1.7]

$$g(\mathbf{x}, \mathbf{x}') := \frac{1}{4\pi \|\mathbf{x} - \mathbf{x}'\|_2}, \quad \mathbf{x} \neq \mathbf{x}'.$$

We recall the standard single and double layer operators defined for smooth densities ψ and $\mathbf{x} \in \mathbb{R}^3 \setminus \Gamma_j$:

$$DL_{0j}(\psi)(\mathbf{x}) := \int_{\Gamma_j} \psi(\mathbf{x}') \nabla g(\mathbf{x}, \mathbf{x}') \cdot \widehat{\mathbf{n}}_{0j} d\Gamma', \quad SL_{0j}(\psi)(\mathbf{x}) := \int_{\Gamma_j} \psi(\mathbf{x}') g(\mathbf{x}, \mathbf{x}') d\Gamma',$$
$$DL_j(\psi)(\mathbf{x}) := \int_{\Gamma_j} \psi(\mathbf{x}') \nabla g(\mathbf{x}, \mathbf{x}') \cdot \widehat{\mathbf{n}}_j d\Gamma', \qquad SL_j(\psi)(\mathbf{x}) := \int_{\Gamma_j} \psi(\mathbf{x}') g(\mathbf{x}, \mathbf{x}') d\Gamma',$$

with the gradient being taken with respect to $\mathbf{r}'$, $\widehat{\mathbf{n}}_j$ being the exterior normal vector of Ω_j. Since for each subdomain the normal is oriented outwardly, it holds that $\widehat{\mathbf{n}}_j = -\widehat{\mathbf{n}}_{0j}$. It can be shown that these operators are linear and continuous (cf. [27, section 3.1], [11, section 3.1]) in the following Sobolev spaces:

$$DL_{0j} : H^{\frac{1}{2}}(\Gamma_j) \to H^1_{loc}\left(\mathbb{R}^3 \setminus \cup_{j=1}^{\mathcal{N}} \Gamma_j\right), \quad SL_{0j} : H^{-\frac{1}{2}}(\Gamma_j) \to H^1_{loc}\left(\mathbb{R}^3 \setminus \cup_{j=1}^{\mathcal{N}} \Gamma_j\right),$$
$$DL_j : H^{\frac{1}{2}}(\Gamma_j) \to H^1_{loc}\left(\mathbb{R}^3 \setminus \cup_{j=1}^{\mathcal{N}} \Gamma_j\right), \quad SL_j : H^{-\frac{1}{2}}(\Gamma_j) \to H^1_{loc}\left(\mathbb{R}^3 \setminus \cup_{j=1}^{\mathcal{N}} \Gamma_j\right).$$

We will write u_j in terms of these boundary potentials, and since we aim at rendering Problem 2.2 onto the cells' boundaries, we will take traces of these potentials. This leads to boundary integral operators (BIOs), which are defined by taking the following averages [27, section 3.1.2]:

$$\begin{aligned}
V^0_{i,j} &:= \frac{1}{2}\left(\gamma^i_D SL_{0j} + \gamma^{0i}_D SL_{0j}\right), & V_j &:= \frac{1}{2}\left(\gamma^{0j}_D SL_j + \gamma^j_D SL_j\right), \\
K^0_{i,j} &:= \frac{1}{2}\left(\gamma^i_D DL_{0j} + \gamma^{0i}_D DL_{0j}\right), & K_j &:= \frac{1}{2}\left(\gamma^{0j}_D DL_j + \gamma^j_D DL_j\right), \\
K^{*0}_{i,j} &:= \frac{1}{2}\left(-\gamma^i_N SL_{0j} + \gamma^{0i}_N SL_{0j}\right), & K^*_j &:= \frac{1}{2}\left(-\gamma^{0j}_N SL_j + \gamma^j_N SL_j\right), \\
W^0_{i,j} &:= -\frac{1}{2}\left(-\gamma^i_N DL_{0j} + \gamma^{0i}_N DL_{0j}\right), & W_j &:= -\frac{1}{2}\left(-\gamma^{0j}_N DL_j + \gamma^j_N DL_j\right).
\end{aligned} \tag{2.5}$$

One can show that these operators are linear and continuous [27, Theorem 3.1.16] in the following Sobolev spaces:

$$\begin{aligned}
V^0_{i,j} &: H^{-\frac{1}{2}}(\Gamma_j) \to H^{\frac{1}{2}}(\Gamma_i), & V_j &: H^{-\frac{1}{2}}(\Gamma_j) \to H^{\frac{1}{2}}(\Gamma_j), \\
W^0_{i,j} &: H^{\frac{1}{2}}(\Gamma_j) \to H^{-\frac{1}{2}}(\Gamma_i), & W_j &: H^{\frac{1}{2}}(\Gamma_j) \to H^{-\frac{1}{2}}(\Gamma_j), \\
K^0_{i,j} &: H^{\frac{1}{2}}(\Gamma_j) \to H^{\frac{1}{2}}(\Gamma_i), & K_j &: H^{\frac{1}{2}}(\Gamma_j) \to H^{\frac{1}{2}}(\Gamma_j), \\
K^{*0}_{i,j} &: H^{-\frac{1}{2}}(\Gamma_j) \to H^{-\frac{1}{2}}(\Gamma_i), & K^*_j &: H^{-\frac{1}{2}}(\Gamma_j) \to H^{-\frac{1}{2}}(\Gamma_j).
\end{aligned}$$

For smooth domains, the jump relations for the potentials across a closed boundary [27, Theorem 3.3.1] yield

$$\begin{aligned}
V^0_{i,j} &= \gamma^{0i}_D SL_{0j}, & V_j &= \gamma^j_D SL_j, \\
W^0_{i,j} &= -\gamma^{0i}_N DL_{0j}, & W_j &= -\gamma^j_N DL_j, \\
K^0_{i,j} &= \gamma^{0i}_D DL_{0j} \text{ with } i \neq j, & K^{*0}_{i,j} &= \gamma^{0i}_N SL_{0j} \text{ with } i \neq j, \\
K^0_{j,j}(\psi) &= \frac{1}{2}\psi + \gamma^{0j}_D DL_{0j}(\psi), & K_j(\psi) &= \frac{1}{2}\psi + \gamma^j_D DL_j(\psi), \\
K^{*0}_{j,j}(\psi) &= -\frac{1}{2}\psi + \gamma^{0j}_N SL_{0j}(\psi), & K^*_j(\psi) &= -\frac{1}{2}\psi + \gamma^j_N SL_j(\psi).
\end{aligned}$$

The next theorem allows us to reconstruct the electric potentials u_j and u_0 from boundary layer operators.

THEOREM 2.3 ([27, section 3]). *The integral representation formulas for* $u_j \in H^1(\Omega_j)$, $u_0 \in H^1_{loc}(\Omega_0)$ *read as*

$$u_0 = -\sum_{i=1}^{\mathcal{N}} DL_{0i}\left(\gamma_D^{0i} u_0\right) + \sum_{i=1}^{\mathcal{N}} SL_{0i}\left(\gamma_N^{0i} u_0\right), \tag{2.6a}$$

$$u_j = -DL_j\left(\gamma_D^j u_j\right) + SL_j\left(\gamma_N^j u_j\right) \quad \forall j \in \{1,\dots,\mathcal{N}\}, \tag{2.6b}$$

where u_j *are zero-valued on the complement of* Ω_j *for* $j = 0,\dots,\mathcal{N}$.

2.3.2. Multiple traces formulation for Problem 2.2. We now write the MTF of Problem 2.2 by taking traces of the integral representation formula (cf. [13] and later references).

For $j \in \{1,\dots,\mathcal{N}\}$, we introduce the Cartesian product of Hilbert spaces $\boldsymbol{H}_j := H^{\frac{1}{2}}(\Gamma_j) \times H^{-\frac{1}{2}}(\Gamma_j)$, with graph norm $\|\cdot\|_{\boldsymbol{H}_j} = \|\cdot\|_{H^{\frac{1}{2}}(\Gamma_j)} + \|\cdot\|_{H^{-\frac{1}{2}}(\Gamma_j)}$. Let be $\boldsymbol{\phi}$, $\boldsymbol{\xi} \in \boldsymbol{H}_j$, such that $\boldsymbol{\phi} = (\phi_D, \phi_N)$ and $\boldsymbol{\xi} = (\xi_D, \xi_N)$. We introduce the cross-product over Γ_j [13, section 2.2.1] by $\langle \boldsymbol{\phi}, \boldsymbol{\xi} \rangle_{\times,j} := \langle \phi_D, \xi_N \rangle_j + \langle \xi_D, \phi_N \rangle_j$, where for brevity we denote $\langle \xi_D, \phi_N \rangle_j := \langle \xi_D, \phi_N \rangle_{H^{\frac{1}{2}}(\Gamma_j) \times H^{-\frac{1}{2}}(\Gamma_j)}$.

We define also the flip-sign operator $\mathsf{X}_j : \boldsymbol{H}_j \to \boldsymbol{H}_j$, $\boldsymbol{\gamma}^{0j} : H^1_{loc}(\Delta, \Omega_0) \to \boldsymbol{H}_j$, and $\boldsymbol{\gamma}^j : H^1(\Delta, \Omega_j) \to \boldsymbol{H}_j$ as

$$\mathsf{X}_j := \begin{bmatrix} I & 0 \\ 0 & -\frac{\sigma_0}{\sigma_j} I \end{bmatrix}, \quad \boldsymbol{\gamma}^{0j} := \begin{pmatrix} \gamma_D^{0j} \\ \gamma_N^{0j} \end{pmatrix}, \quad \text{and } \boldsymbol{\gamma}^j := \begin{pmatrix} \gamma_D^j \\ \gamma_N^j \end{pmatrix}, \quad j \in \{1,\dots,\mathcal{N}\}, \tag{2.7}$$

with I being the identity operator understood in the corresponding functional space. Then, we succinctly write Dirichlet and Neumann boundary conditions, (2.2c) and (2.2d), respectively, as

$$-\mathsf{X}_j \boldsymbol{\gamma}^{0j} u_0 + \boldsymbol{\gamma}^j u_j = \mathsf{X}_j (v_j,\ 0)^t + \mathsf{X}_j \boldsymbol{\gamma}^{0j} \phi_e, \tag{2.8a}$$

$$\boldsymbol{\gamma}^{0j} u_0 - \mathsf{X}_j^{-1} \boldsymbol{\gamma}^j u_j = -(v_j,\ 0)^t - \boldsymbol{\gamma}^{0j} \phi_e, \tag{2.8b}$$

with superscript t denoting transposition, and where both equations are equivalent. Taking Dirichlet and Neumann traces of both (2.6a) and (2.6b), and rewriting in terms of BIOs, we obtain

$$\begin{aligned}
\gamma_D^{0j} u_0 &= -\left(-\frac{1}{2} I\left(\gamma_D^{0j} u_0\right) + \sum_{i=1}^{n} K_{j,i}^0\left(\gamma_D^{0i} u_0\right)\right) + \sum_{i=1}^{n} V_{j,i}^0\left(\gamma_N^{0i} u_0\right), \\
\gamma_N^{0j} u_0 &= \sum_{i=1}^{n} W_{j,i}^0\left(\gamma_D^{0i} u_0\right) + \left(\frac{1}{2} I\left(\gamma_N^{0j} u_0\right) + \sum_{i=1}^{n} K_{j,i}^{*0}\left(\gamma_N^{0i} u_0\right)\right), \\
\gamma_D^j u_j &= -\left(-\frac{1}{2} I\left(\gamma_D^j u_j\right) + K_j\left(\gamma_D^j u_j\right)\right) + V_j\left(\gamma_N^j u_j\right), \\
\gamma_N^j u_j &= W_j\left(\gamma_D^j u_j\right) + \left(\frac{1}{2} I\left(\gamma_N^j u_j\right) + K_j^*\left(\gamma_N^j u_j\right)\right).
\end{aligned}$$

After some algebra, one can write

$$\boldsymbol{\gamma}^{0j} u_0 = 2 \sum_{i=1}^{\mathcal{N}} \mathsf{A}_{j,i}^0 \boldsymbol{\gamma}^{0i} u_0, \quad \boldsymbol{\gamma}^j u_j = 2\, \mathsf{A}_j \boldsymbol{\gamma}^j u_j, \quad j \in \{1,\dots,\mathcal{N}\},$$

with $\mathsf{A}_{j,i}^0 := \left[\begin{smallmatrix} -K_{j,i}^0 & V_{j,i}^0 \\ W_{j,i}^0 & K_{j,i}^{*0} \end{smallmatrix}\right]$ and $\mathsf{A}_j := \left[\begin{smallmatrix} -K_j & V_j \\ W_j & K_j^* \end{smallmatrix}\right]$. By substituting $\boldsymbol{\gamma}^{0j} u_0$, $\boldsymbol{\gamma}^j u_j$ into (2.8b) and (2.8a), we obtain

$$2\sum_{i=1}^{n}\mathsf{A}^0_{j,i}\boldsymbol{\gamma}^{0i}u_0-\mathsf{X}_j^{-1}\boldsymbol{\gamma}^j u_j=-(v_j,\ 0)^t-\boldsymbol{\gamma}^{0j}\phi_e,$$
$$-\mathsf{X}_j\boldsymbol{\gamma}^{0j}u_0+2\,\mathsf{A}_j\,\boldsymbol{\gamma}^j u_j=\mathsf{X}_j(v_j,\ 0)^t+\mathsf{X}_j\boldsymbol{\gamma}^{0j}\phi_e\quad\text{ on }\Gamma_j.$$

We define the Cartesian product space of multiple traces $\mathbb{H}:=\Pi_{j=1}^{\mathcal{N}}\boldsymbol{H}_j$ and $\mathbb{H}^{(2)}:=\mathbb{H}\times\mathbb{H}=\Pi_{j=1}^{\mathcal{N}}\boldsymbol{H}_j\times\Pi_{j=1}^{\mathcal{N}}\boldsymbol{H}_j$; the multiple trace spaces reordering $\mathbb{H}_D:=\Pi_{j=1}^{\mathcal{N}}H^{\frac{1}{2}}(\Gamma_j)$, $\mathbb{H}_N:=\Pi_{j=1}^{\mathcal{N}}H^{-\frac{1}{2}}(\Gamma_j)$; and the cross-product

$$\langle\boldsymbol{\phi},\boldsymbol{\xi}\rangle_\times=\sum_{j=1}^{\mathcal{N}}\langle\boldsymbol{\phi}^{0j},\boldsymbol{\xi}^{0j}\rangle_{\times,j}+\sum_{j=1}^{\mathcal{N}}\langle\boldsymbol{\phi}^{j},\boldsymbol{\xi}^{j}\rangle_{\times,j},$$

with $\boldsymbol{\phi}=(\boldsymbol{\phi}^{01},\dots,\boldsymbol{\phi}^{0\mathcal{N}},\boldsymbol{\phi}^{1},\dots,\boldsymbol{\phi}^{\mathcal{N}})$ and $\boldsymbol{\xi}=(\boldsymbol{\xi}^{01},\dots,\boldsymbol{\xi}^{0\mathcal{N}},\boldsymbol{\xi}^{1},\dots,\boldsymbol{\xi}^{\mathcal{N}})$.

The local MTF operator [13, section 3.2.3] $\mathbf{M}_{\mathcal{N}}:\mathbb{H}^{(2)}\to\mathbb{H}^{(2)}$ for the problem presented in section 2 takes the form

$$\mathbf{M}_{\mathcal{N}}:=\begin{bmatrix}2\mathbf{A}_{0,\mathcal{N}} & -\mathbf{X}_{\mathcal{N}}^{-1}\\ -\mathbf{X}_{\mathcal{N}} & 2\mathbf{A}_{1,\mathcal{N}}\end{bmatrix},\ \text{with }\mathbf{A}_{0,\mathcal{N}}:=\begin{bmatrix}\mathsf{A}^0_{1,1} & \mathsf{A}^0_{1,2} & \dots & \mathsf{A}^0_{1,\mathcal{N}}\\ \mathsf{A}^0_{2,1} & \mathsf{A}^0_{2,2} & \dots & \mathsf{A}^0_{2,\mathcal{N}}\\ \vdots & & \ddots & \vdots\\ \mathsf{A}^0_{\mathcal{N},1} & \mathsf{A}^0_{\mathcal{N},2} & \dots & \mathsf{A}^0_{\mathcal{N},\mathcal{N}}\end{bmatrix},\tag{2.9}$$

and diagonal operators $\mathbf{A}_{1,\mathcal{N}}:=\operatorname{diag}(\mathsf{A}_1,\dots,\mathsf{A}_{\mathcal{N}})$ and $\mathbf{X}_{\mathcal{N}}:=\operatorname{diag}(\mathsf{X}_1,\dots\mathsf{X}_{\mathcal{N}})$. With the MTF operator, the interface conditions (2.2b), (2.2c), and (2.2d) (Problem 2.2) can be written as

$$\mathbf{M}_{\mathcal{N}}\begin{pmatrix}\boldsymbol{\gamma}^0_u\\ \boldsymbol{\gamma}_u\end{pmatrix}=\begin{pmatrix}-\mathbf{I}_{2\mathcal{N}\times\mathcal{N}}\,\mathbf{v}\\ \mathbf{X}_{\mathcal{N}}\,\mathbf{I}_{2\mathcal{N}\times\mathcal{N}}\,\mathbf{v}\end{pmatrix}+\begin{pmatrix}-\boldsymbol{\gamma}^0_{\phi_e}\\ \mathbf{X}_{\mathcal{N}}\,\boldsymbol{\gamma}^0_{\phi_e}\end{pmatrix},\tag{2.10}$$

where we use the notation

$$\boldsymbol{\gamma}^0_u:=\left(\boldsymbol{\gamma}^{01}u_0,\boldsymbol{\gamma}^{02}u_0,\dots,\boldsymbol{\gamma}^{0\mathcal{N}}u_0\right)^t,\qquad \boldsymbol{\gamma}_u:=\left(\boldsymbol{\gamma}^{1}u_1,\boldsymbol{\gamma}^{2}u_2,\dots,\boldsymbol{\gamma}^{\mathcal{N}}u_{\mathcal{N}}\right)^t,$$
$$\boldsymbol{\gamma}^0_{\phi_e}:=\left(\boldsymbol{\gamma}^{01}\phi_e,\boldsymbol{\gamma}^{02}\phi_e,\dots,\boldsymbol{\gamma}^{0\mathcal{N}}\phi_e\right)^t,\qquad \mathbf{v}:=\left(v_1,v_2,v_3,\dots,v_{\mathcal{N}}\right)^t,$$

and the operator $\mathbf{I}_{2\mathcal{N}\times\mathcal{N}}:\mathbb{H}_D\to\mathbb{H}$ defined as

$$\mathbf{I}_{2\mathcal{N}\times\mathcal{N}}:=\begin{pmatrix}I & 0 & \dots & 0\\ 0 & 0 & \dots & 0\\ 0 & I & \dots & 0\\ 0 & 0 & \dots & 0\\ \vdots & \vdots & & \vdots\\ 0 & 0 & \dots & I\\ 0 & 0 & \dots & 0\end{pmatrix}.$$

Notice that the identity operators act on the corresponding Dirichlet traces.

The following result is a consequence of [11, Propositions 3.9 and 3.10] along with the Fredholm alternative.

THEOREM 2.4 (existence, uniqueness, and stability). *The operator $\mathbf{M}_{\mathcal{N}}$ is a linear, injective, and coercive operator in $\mathbb{H}^{(2)}$. For all $\boldsymbol{\xi}\in\mathbb{H}^{(2)}$, there exists a unique weak solution $\boldsymbol{\lambda}\in\mathbb{H}^{(2)}$ of*

$$(\mathbf{M}_{\mathcal{N}}\boldsymbol{\lambda},\boldsymbol{\phi})_\times=(\boldsymbol{\xi},\boldsymbol{\phi})_\times\quad\forall\boldsymbol{\phi}\in\mathbb{H}^{(2)}$$

that satisfies the stability estimate $\|\boldsymbol{\lambda}\|_{\mathbb{H}^{(2)}}\le c\|\boldsymbol{\xi}\|_{\mathbb{H}^{(2)}}$ for a constant $c>0$.

2.3.3. Boundary integral formulation of Problem 2.2. Until this point, we have not introduced the membrane dynamics of Problem 2.2. In the following, we will use the theory presented in [12, 11] to combine the MTF with the nonlinear dynamics. Indeed, thanks to Theorem 2.4 we can take the inverse of the MTF operator, and (2.10) becomes

$$\begin{pmatrix}\boldsymbol{\gamma}_u^0\\ \boldsymbol{\gamma}_u\end{pmatrix} = \mathbf{M}_{\mathcal{N}}^{-1}\begin{pmatrix}-\mathbf{I}_{2\mathcal{N}\times\mathcal{N}}\,\mathbf{v}\\ \mathbf{X}_{\mathcal{N}}\,\mathbf{I}_{2\mathcal{N}\times\mathcal{N}}\,\mathbf{v}\end{pmatrix} + \mathbf{M}_{\mathcal{N}}^{-1}\begin{pmatrix}-\boldsymbol{\gamma}_{\phi_e}^0\\ \mathbf{X}_{\mathcal{N}}\,\boldsymbol{\gamma}_{\phi_e}^0\end{pmatrix}.$$

The even components of the vector γ_u (the interior Neumann traces), related to the nonlinear dynamics of the problem by (2.2e), can be retrieved as follows:

$$\begin{pmatrix}\sigma_1\gamma_N^1(u_1)\\ \sigma_2\gamma_N^2(u_2)\\ \vdots\\ \sigma_{\mathcal{N}}\gamma_N^{\mathcal{N}}(u_{\mathcal{N}})\end{pmatrix} = \boldsymbol{\sigma}_{\mathcal{N}\times 4\mathcal{N}}\mathbf{M}_{\mathcal{N}}^{-1}\left(\begin{pmatrix}-\mathbf{I}_{2\mathcal{N}\times\mathcal{N}}\,\mathbf{v}\\ \mathbf{X}_{\mathcal{N}}\,\mathbf{I}_{2\mathcal{N}\times\mathcal{N}}\,\mathbf{v}\end{pmatrix} + \begin{pmatrix}-\boldsymbol{\gamma}_{\phi_e}^0\\ \mathbf{X}_{\mathcal{N}}\,\boldsymbol{\gamma}_{\phi_e}^0\end{pmatrix}\right),$$

where the dimensions of $\boldsymbol{\sigma}_{\mathcal{N}\times 4\mathcal{N}}$ are $\mathcal{N}\times 4\mathcal{N}$, the first half containing only zeros:

$$\boldsymbol{\sigma}_{\mathcal{N}\times 4\mathcal{N}} := \begin{pmatrix}0 & \dots & 0 & \sigma_1 I & 0 & 0 & \dots & 0\\ 0 & \dots & 0 & 0 & 0 & \sigma_2 I & \dots & 0\\ \vdots & & \vdots & \vdots & \vdots & \vdots & & \vdots\\ 0 & \dots & 0 & 0 & 0 & 0 & \dots & \sigma_{\mathcal{N}} I\end{pmatrix}.$$

Now, we define the Dirichlet-to-Neumann operators $\mathcal{J}_{\mathcal{N}} : \mathbb{H}_D \to \mathbb{H}_N$ and $\Phi : H^1_{loc}(\Omega_0) \to \mathbb{H}_N$ as

(2.11)
$$\mathcal{J}_{\mathcal{N}}(\mathbf{v}) := \boldsymbol{\sigma}_{\mathcal{N}\times 4\mathcal{N}}\mathbf{M}_{\mathcal{N}}^{-1}\begin{pmatrix}-\mathbf{I}_{2\mathcal{N}\times\mathcal{N}}\,\mathbf{v}\\ \mathbf{X}_{\mathcal{N}}\,\mathbf{I}_{2\mathcal{N}\times\mathcal{N}}\,\mathbf{v}\end{pmatrix} \quad\text{and}\quad \Phi(\phi_e) := \boldsymbol{\sigma}_{\mathcal{N}\times 4\mathcal{N}}\mathbf{M}_{\mathcal{N}}\begin{pmatrix}-\boldsymbol{\gamma}_{\phi_e}^0\\ \mathbf{X}_{\mathcal{N}}\,\boldsymbol{\gamma}_{\phi_e}^0\end{pmatrix}.$$

THEOREM 2.5 (Lemma 4.3 in [11]). *The operator $\mathcal{J}_{\mathcal{N}} : \mathbb{H}_D \to \mathbb{H}_N$ is continuous and coercive.*

Now we can finally rewrite[4] Problem 2.2 as an abstract parabolic equation on Γ_j.

PROBLEM 2.6. *Let us assume the following as given: a final time $T \in \mathbb{R}^+$, an external potential $\phi_e \in C([0,T], H^1_{loc}(\Omega_0))$, and initial conditions $v_j(0) = v_0 \in H^{\frac{1}{2}}(\Gamma_j)$, $Z_j(0) = Z_j^0 \in H^{\frac{1}{2}}(\Gamma_j)$ for $j \in \{1,\dots,\mathcal{N}\}$. We seek $\mathbf{v} = (v_1,\dots,v_{\mathcal{N}})^t$, with $v_j \in C([0,T], H^{\frac{1}{2}}(\Gamma_j))$, and $\mathbf{Z} = (Z_1,\dots,Z_{\mathcal{N}})^t$, $Z_j \in C([0,T], H^{\frac{1}{2}}(\Gamma_j))$, for $j \in \{1,\dots,\mathcal{N}\}$, such that*

$$\mathbf{C_m}\partial_t\mathbf{v} = -\mathbf{I}^{ep}(\mathbf{v},\mathbf{Z}) - \mathcal{J}_{\mathcal{N}}(\mathbf{v}) - \Phi(\phi_e) \text{ on } [0,T]\times\Gamma_j, \tag{2.12}$$

where $\mathbf{C_m}$ is a diagonal matrix $\operatorname{diag}(c_{m,1},\dots,c_{m,\mathcal{N}})$ *and the operators $\mathcal{J}_{\mathcal{N}}(\mathbf{v})$ and $\Phi(\phi_e)$ are defined in* (2.11). *The vector $\mathbf{I}^{ep}(\mathbf{v},\mathbf{Z}) = (I_1^{ep}(v_1,Z_1),\dots,I_{\mathcal{N}}^{ep}(v_{\mathcal{N}},Z_{\mathcal{N}}))^t$ satisfies* (2.3), (2.4), *and* (2.1).

[4]The MTF (2.9) is almost equal to the one in [11] and [12]. Specifically, (2.9) is multiplied by a factor two and the first row does not have a factor σ_j as in [12] and [11].

3. Numerical approximation. In this section we propose a numerical solution of Problem 2.6. We use a multistep semi-implicit time scheme or implicit-explicit method (IMEX), similar to one used in [12, 11] (see section 3.1). For the space discretization, we follow an approach analogous to the two-dimensional case presented in [11] using spherical harmonics. Since we do not work with complex-valued functions, we employ real spherical harmonics to approximate boundary unknowns. We recall that our dynamic model leads to poorly regular solutions in time.

3.1. Multistep semi-implicit time scheme. Let $\mathcal{T}_S := \{t_s\}_{s=0}^{S}$ denote the uniform partition of the time interval $[0,T]$, with $T \in \mathbb{R}^+$ and $S \in \mathbb{N}$, where the time step is $\tau = T/S$ and $t_s = s\tau$. Write

$$t_{s+\frac{1}{2}} := t_s + \frac{\tau}{2}, \quad s \in \{0,\dots,S-1\},$$

for the mid-step between t_s and t_{s+1}. For a time-dependent quantity $\phi(t)$, we write $\phi^{(s)} = \phi(t_s)$, and we define the following quantities

$$\phi^{(s+\frac{1}{2})} := \phi(t_{s+\frac{1}{2}}), \qquad \overline{\phi}^{(s+\frac{1}{2})} := \frac{\phi^{(s+1)} + \phi^{(s)}}{2},$$
$$\hat{\phi}^{(s+\frac{1}{2})} := \frac{3\phi^{(s)} - \phi^{(s-1)}}{2}, \qquad \overline{\partial}\phi^{(s)} := \frac{\phi^{(s+1)} - \phi^{(s)}}{\tau}.$$

With these, we approximate in time (2.6) and (2.4) as follows:

$$\mathbf{C_m}\overline{\partial}\mathbf{v}^{(s)} = -\mathbf{I}^{ep}\left(\widehat{\mathbf{v}}^{(s+\frac{1}{2})}, \widehat{\mathbf{Z}}^{(s+\frac{1}{2})}\right) - \mathcal{J}_{\mathcal{N}}\left(\overline{\mathbf{v}}^{(s+\frac{1}{2})}\right) - \Phi(\phi_e^{(s+\frac{1}{2})}),$$
$$\overline{\partial}^{(s)} Z_j = \max\left(\frac{\beta_j(\widehat{v}_j^{(s+\frac{1}{2})}) - \widehat{Z_j}^{(s+\frac{1}{2})}}{\tau_{ep,j}}, \frac{\beta_j(\widehat{v}_j^{(s+\frac{1}{2})}) - \widehat{Z_j}^{(s+\frac{1}{2})}}{\tau_{res,j}}\right).$$

From these expressions, we can notice the following:

(i) At each iteration, the approximation at t_{s+1} requires two previous steps, t_s and t_{s-1}, but we only have information about the time t_0. Thus, we will estimate the values for the time t_1 with a predictor-corrector algorithm introduced later in this section.

(ii) Provided with values for the two previous time steps, unknowns for the next time are obtained in terms of $\overline{\partial}\mathbf{v}^{(s)}$, $\overline{\mathbf{v}}^{(s+\frac{1}{2})}$, and $\overline{\partial}^{(s)}$, which are linear. Nonlinear terms are evaluated with values already known, i.e., they are explicit terms, unlike the others. Hence, we use the adjective semi-implicit or IMEX for the multistep method employed.

(iii) At each time step, the discrete problem to be solved is linear. One could choose time-domain schemes with implicit nonlinear parts. However, more information about $\mathbf{I}^{ep}$ may be needed. In contrast, our semi-implicit time only requires us to evaluate the function $\mathbf{I}^{ep}$.

The predictor-corrector algorithm can be found in detail in [29, Chapter 13], [12, Algorithm 1]. Set $\mathbf{w}^{(0)} = \mathbf{v}^{(0)}$ and $\mathbf{Q}^{(0)} = \mathbf{Z}(0)$. Then, proceed as follows:

(I) *Predictor.* First, construct predictions $\mathbf{w}^{(1)}$ and $\mathbf{Q}^{(1)}$ by solving

$$\mathbf{C_m}\overline{\partial}\mathbf{w}^{(0)} = -\mathbf{I}^{ep}\left(\mathbf{w}^{(0)}, \mathbf{Q}^{(0)}\right) - \mathcal{J}_{\mathcal{N}}\left(\overline{\mathbf{w}}^{(\frac{1}{2})}\right) - \Phi\left(\phi_e^{(\frac{1}{2})}\right),$$
$$\overline{\partial}Q_j^{(0)} = \max\left(\frac{\beta_j(w_j^{(0)}) - Q_j^{(0)}}{\tau_{ep,j}}, \frac{\beta_j(w_j^{(0)}) - Q_j^{(0)}}{\tau_{res,j}}\right) \quad \forall j \in \{1,\dots,\mathcal{N}\}.$$

(II) *Corrector.* Then, correct $\mathbf{w}^{(1)}$ and $\mathbf{Q}^{(1)}$ to obtain final values for $\mathbf{v}^{(1)}$ and $\mathbf{Z}^{(1)}$ through

$$\mathbf{C_m}\overline{\partial}\mathbf{v}^{(0)} = -\mathbf{I}^{ep}\left(\widehat{\mathbf{w}}^{(\frac{1}{2})}, \widehat{\mathbf{Q}}^{(\frac{1}{2})}\right) - \mathcal{J}_{\mathcal{N}}\left(\overline{\mathbf{v}}^{(\frac{1}{2})}\right) - \Phi\left(\phi_e^{(\frac{1}{2})}\right),$$
$$\overline{\partial}^{(0)} Z_j = \max\left(\frac{\beta_j(\widehat{w}_j^{(\frac{1}{2})}) - \widehat{Q_j}^{(\frac{1}{2})}}{\tau_{ep,j}}, \frac{\beta_j(\widehat{w}_j^{(\frac{1}{2})}) - \widehat{Q_j}^{(\frac{1}{2})}}{\tau_{res,j}}\right) \quad \forall j \in \{1,\dots,\mathcal{N}\}.$$

Then, from the corrector equations, $\mathbf{v}^{(1)}$ and $\mathbf{Z}^{(1)}$ are obtained implicitly.

Remark 3.1. The predictor-corrector algorithm is only used for obtaining the first time step, as required by the multistep semi-implicit time scheme. One could think of a predictor-corrector algorithm at all time steps, but this would entail a higher computational cost and reassess the theoretical convergence results in [12].

Finally, before tackling the spatial discretization, we recall the following result.

THEOREM 3.2 ([12, Lemma 7]). *Let $\phi \in C^2([0,T]; L^2(\Gamma_j))$, $j \in \{1,\dots,\mathcal{N}\}$; then it holds that*

$$\left\|\overline{\phi}^{(s+\frac{1}{2})} - \phi^{(s+\frac{1}{2})}\right\|_{L^2(\Gamma_j)} \leq \frac{\tau^2}{4} \max_{t\in[t_s,t_{s+1}]} \left\|\partial_t^2\phi(t)\right\|_{L^2(\Gamma_j)},$$
$$\left\|\hat{\phi}^{(s+\frac{1}{2})} - \phi^{(s+\frac{1}{2})}\right\|_{L^2(\Gamma_j)} \leq \frac{5\tau^2}{16} \max_{t\in[t_{s-1},t_{s+1}]} \left\|\partial_t^2\phi(t)\right\|_{L^2(\Gamma_j)}.$$

3.2. Spatial discretization. We now spatially discretize Problem 2.6. We start by introducing real spherical harmonics used as the spatial basis for the Dirichlet and Neumann traces (3.3). Then, we proceed with BIO discretization (see Theorem 3.4). Finally, the multistep semi-explicit time method and the spatial discretization are combined into a fully discrete scheme (see Problem (3.8)).

3.2.1. Spherical coordinates and spherical harmonics. A vector is written as $\mathbf{r} = (r,\varphi,\theta)^t$, with $r \in [0,\infty)$, $\varphi \in [0,2\pi)$, and $\theta \in [0,\pi]$, which in Cartesian coordinates is equivalent to $\mathbf{r} = r\,(\sin\theta\cos\varphi, \sin\theta\sin\varphi, \cos\theta)^t$. Spherical harmonics of degree l and order m are defined using spherical coordinates as in [31, section 2], [7, Example 4.3.33]:

$$Y_{l,m}(\theta,\varphi) := \sqrt{(2-\delta_{m,0})\frac{(2l+1)\,(l-m)!}{4\pi\,(l+m)!}} P_l^m(\cos\theta)\cos m\varphi, \text{ and} \tag{3.1a}$$

$$Y_{l,-m}(\theta,\varphi) := \sqrt{(2-\delta_{m,0})\frac{(2l+1)\,(l-m)!}{4\pi\,(l+m)!}} P_l^m(\cos\theta)\sin m\varphi, \tag{3.1b}$$

with $l \in \mathbb{N}_0$, $m \in \mathbb{Z}$ such that $0 \leq m \leq l$. If $m = 0$, $\delta_{m,0} = 1$, and it is zero otherwise. P_l^m are the associated Legendre functions of degree l and order m defined as

$$P_l^m(x) := (-1)^m\left(1-x^2\right)^{\frac{m}{2}} \frac{d^m}{dx^m} P_l(x), \quad \text{with} \quad P_l(x) := \frac{1}{2^l l!}\frac{d^l}{dx^l}(x^2-1)^l.$$

Here, the term $(-1)^m$ is the Condon–Shortley phase factor. Spherical harmonics are dense in $C(\mathbb{S}^2)$, with $\mathbb{S}^2$ the surface of the unit sphere, and form a complete orthonormal system in $L^2(\mathbb{S}^2)$ [8, sections 7.3 and 7.5].

Let be $j \in \{1,\dots,\mathcal{N}\}$. We define the reference system j as the one centered at $\mathbf{p_j}$ with the same orientation as the system centered at the origin. Furthermore, we

denote by $Y_{l,m,j}$ the spherical harmonic $Y_{l,m}$ centered at the origin of the jth reference system. Thus, if $(r_j, \varphi_j, \theta_j)$ are the vector spherical coordinates of $\mathbf{r_j}$ in the reference system j, we have that $Y_{l,m,j}(\mathbf{r}_j) = Y_{l,m}(\theta_j, \varphi_j)$.

For $L \in \mathbb{N}_0$ and $j \in \{1, \ldots, \mathcal{N}\}$, we define subspaces

$$\mathcal{Y}_L(\Gamma_j) := \operatorname{span}\{Y_{l,m,j} : l \in \mathbb{N}_0, m \in \mathbb{Z}, l \le L, |m| \le l\}, \tag{3.2}$$

equipped with the $L^2(\Gamma_j)$-norm. Notice that the dimension of each subspace is $(L+1)^2$, and that the sequence of subspaces $\{\mathcal{Y}_L(\Gamma_j)\}_{L\in\mathbb{N}_0}$ is dense in $H^{\frac{1}{2}}(\Gamma_j)$ and in $H^{-\frac{1}{2}}(\Gamma_j)$. The result follows from the density of spherical harmonics in the spaces of continuous functions. This last result justifies the discretization of all boundary Dirichlet and Neumann unknowns with spherical harmonics. At a given time t, for $j \in \{1, \ldots, \mathcal{N}\}$, we write $u^L_{D,0j}$, $u^L_{N,0j}$, $u^L_{D,j}$, $u^L_{N,j}$, v^L_j, and Z^L_j in $\mathcal{Y}_L(\Gamma_j)$ for the approximations of $\gamma^{0j}_D u_0$, $\gamma^{0j}_N u_0$, $\gamma^j_D u_j$, $\gamma^j_N u_j$, v_j, and Z_j, respectively. They can be written as the following series expansions:

$$u^L_{D,0j} = \sum_{l=0}^{L}\sum_{m=-l}^{l} u^{l,m}_{D,0j} Y_{l,m,j}, \qquad u^L_{N,0j} = \sum_{l=0}^{L}\sum_{m=-l}^{l} u^{l,m}_{N,0j} Y_{l,m,j}, \tag{3.3a}$$

$$u^L_{D,j} = \sum_{l=0}^{L}\sum_{m=-l}^{l} u^{l,m}_{D,j} Y_{l,m,j}, \qquad u^L_{N,j} = \sum_{l=0}^{L}\sum_{m=-l}^{l} u^{l,m}_{N,j} Y_{l,m,j}, \tag{3.3b}$$

$$v^L_j = \sum_{l=0}^{L}\sum_{m=-l}^{l} v^{l,m}_j Y_{l,m,j}, \qquad Z^L_j = \sum_{l=0}^{L}\sum_{m=-l}^{l} Z^{l,m}_j Y_{l,m,j} \tag{3.3c}$$

with $u^{l,m}_{D,0j}$, $u^{l,m}_{N,0j}$, $u^{l,m}_{D,j}$, $u^{l,m}_{N,j}$, $v^{l,m}_j$, and $Z^{l,m}_j$ being constants in space but varying in time. Notice that the norm in $\mathcal{Y}_L(\Gamma_j)$ of any of these functions is the square root of the sum of squared coefficients times the radius of Γ_j, i.e.,

$$\left\|v^L_j\right\|^2_{\mathcal{Y}_L(\Gamma_j)} = R_j \sum_{l=0}^{L}\sum_{m=-l}^{l} (v^{l,m}_j)^2. \tag{3.4}$$

Finally, let $\mathbb{Y}_L := \Pi_{j=1}^{\mathcal{N}} \mathcal{Y}_{\mathcal{L}}(\Gamma_j)$, and define the following vectors in $\mathbb{Y}_L$:

$$\mathbf{v}^L := \left(v^L_1, \ldots, v^L_j, \ldots, v^L_{\mathcal{N}}\right)^t, \qquad \mathbf{Z}^L := \left(z^L_1, \ldots, Z^L_j, \ldots, z^L_{\mathcal{N}}\right)^t, \tag{3.5a}$$

$$\mathbf{u}^L_{D,0} := \left(u^L_{D,01}, \ldots, u^L_{D,0j}, \ldots, u^L_{D,0\mathcal{N}}\right)^t, \quad \mathbf{u}^L_D := \left(u^L_{D,1}, \ldots, u^L_{D,j}, \ldots, u^L_{D,\mathcal{N}}\right)^t, \tag{3.5b}$$

$$\mathbf{u}^L_{N,0} := \left(u^L_{N,01}, \ldots, u^L_{N,0j}, \ldots, u^L_{N,0\mathcal{N}}\right)^t, \quad \mathbf{u}^L_D := \left(u^L_{N,1}, \ldots, u^L_{N,j}, \ldots, u^L_{N,\mathcal{N}}\right)^t. \tag{3.5c}$$

The norm for a function in $\mathbb{Y}_L$, for example, $\mathbf{v}^L$, is $\|\mathbf{v}^L\|^2_{\mathbb{Y}_L} = \sum_{j=1}^{\mathcal{N}} \|v^L_j\|^2_{\mathcal{Y}_L(\Gamma_j)}$.

3.2.2. BIO discretization. The fundamental solution can be expanded using spherical harmonics [7, Theorem 4.3.29, Lemma 4.4.1, and Remark 4.4.2], as the following result shows.

THEOREM 3.3. *Let* $\mathbf{r}$, $\mathbf{r}'$ *be vectors whose spherical coordinates in the reference system* j *are* $(r_j, \theta_j, \varphi_j)$ *and* $\left(r'_j, \theta'_j, \varphi'_j\right)$, *respectively. For* $r_j > r'_j$ *we have that*

$$g(\mathbf{r}, \mathbf{r}') = \sum_{l=0}^{\infty} \frac{1}{2l+1} \frac{r'^l_j}{r^{l+1}_j} \sum_{m=-l}^{l} Y_{l,m,j}(\mathbf{r}) Y_{l,m,j}(\mathbf{r}'). \tag{3.6}$$

Moreover, the series (3.6) *and its term-by-term first derivatives with respect to* r_j *or* r'_j *are absolutely and uniformly convergent on compact subsets with* $r_j > r'_j$ [6, *section* 2.3, *pp.* 23 *and* 24].

THEOREM 3.4. *The diagonal forms of the BIOs* (2.5) *are*

$$V^0_{j,j}\left(Y_{l,m,j}\right) = \frac{1}{2l+1} R_j Y_{l,m,j}, \qquad V_j\left(Y_{l,m,j}\right) = \frac{1}{2l+1} R_j Y_{l,m,j},$$
$$K^0_{j,j}\left(Y_{l,m,j}\right) = \frac{1}{2(2l+1)} Y_{l,m,j}, \qquad K_j\left(Y_{l,m,j}\right) = -\frac{1}{2(2l+1)} Y_{l,m,j},$$
$$K^{*0}_{j,j}\left(Y_{l,m,j}\right) = \frac{1}{2l+1} Y_{l,m,j}, \qquad K^*_j\left(Y_{l,m,j}\right) = -\frac{1}{2(2l+1)} Y_{l,m,j},$$
$$W^0_{j,j}\left(Y_{l,m,j}\right) = \frac{l(l+1)}{2l+1}\frac{1}{R_j} Y_{l,m,j}, \qquad W_j\left(Y_{l,m,j}\right) = \frac{l(l+1)}{2l+1}\frac{1}{R_j} Y_{l,m,j}.$$

Proof. The result follows from Theorem 3.3, the orthonormality of spherical harmonics, and the definitions of the BIOs presented in (2.5). Similar diagonal forms can also be found in [30, section 3 and Table 2], where the result is stated for complex spherical harmonics on the unit sphere. ∎

COROLLARY 3.5. *The following holds:*

$$\left(V^0_{j,j}\left(Y_{l,m,j}\right), Y_{p,q,j}\right)_{L^2(\Gamma_j)} = \left(V_j\left(Y_{l,m,j}\right), Y_{p,q,j}\right)_{L^2(\Gamma_j)} = \frac{R_j^3}{2l+1}\delta_{l,p}\delta_{m,q},$$
$$\left(K^0_{j,j}\left(Y_{l,m,j}\right), Y_{p,q,j}\right)_{L^2(\Gamma_j)} = -\left(K_j\left(Y_{l,m,j}\right), Y_{p,q,j}\right)_{L^2(\Gamma_j)} = \frac{R_j^2}{2(2l+1)}\delta_{l,p}\delta_{m,q},$$
$$\left(K^{*0}_{j,j}\left(Y_{l,m,j}\right), Y_{p,q,j}\right)_{L^2(\Gamma_j)} = -\left(K^*_j\left(Y_{l,m,j}\right), Y_{p,q,j}\right)_{L^2(\Gamma_j)} = \frac{R_j^2}{2(2l+1)}\delta_{l,p}\delta_{m,q},$$
$$\left(W^0_{j,j}\left(Y_{l,m,j}\right), Y_{p,q,j}\right)_{L^2(\Gamma_j)} = \left(W_j\left(Y_{l,m,j}\right), Y_{p,q,j}\right)_{L^2(\Gamma_s)} = \frac{l(l+1)}{2l+1} R_j \delta_{l,p}\delta_{m,q},$$

with $\delta_{l,p}$, $\delta_{m,q}$ *denoting the standard Kronecker deltas. Also, for the scalar identity operators presented in section* 2.3*, it holds that* $(I(Y_{l,m,j}), Y_{p,q,j})_{L^2(\Gamma_j)} = R_j^2 \delta_{l,p}\delta_{m,q}$.

Cross-interaction operators, e.g., $V^0_{i,j}$ for $i \neq j$, are nonsingular and generally nondiagonalizable. The double and single layer operators' analytic expressions can be used to compute the nonsingular integrals for $i \neq j$:

$$\left(V^0_{i,j}\left(Y_{l,m,j}\right); Y_{p,q,i}\right)_{L^2(\Gamma_i)} = \int_{\Gamma_i} SL_{0j}(Y_{l,m,j}) Y_{p,q,i}\, d\Gamma_i, \tag{3.7a}$$
$$\left(K^0_{i,j}\left(Y_{l,m,j}\right); Y_{p,q,i}\right)_{L^2(\Gamma_i)} = \int_{\Gamma_i} DL_{0j}(Y_{l,m,j}) Y_{p,q,i}\, d\Gamma_i, \tag{3.7b}$$
$$\left(K^{*0}_{i,j}\left(Y_{l,m,j}\right); Y_{p,q,i}\right)_{L^2(\Gamma_i)} = \int_{\Gamma_i} \widehat{\mathbf{n}}_{0i} \cdot \nabla SL_{0j}(Y_{l,m,j}) Y_{p,q,i}\, d\Gamma_i, \tag{3.7c}$$
$$\left(W^0_{i,j}\left(Y_{l,m,j}\right); Y_{p,q,i}\right)_{L^2(\Gamma_i)} = -\int_{\Gamma_i} \widehat{\mathbf{n}}_{0i} \cdot \nabla DL_{0j}(Y_{l,m,j}) Y_{p,q,i}\, d\Gamma_i. \tag{3.7d}$$

Approximations of the integrals (3.7) are provided via Gauss–Legendre quadratures. Specifically, along θ, we use the change of variable $u = \cos\theta$. Then, variable functions are sampled at the zeros of the Legendre polynomial of degree L_c+1, whereas the trapezoidal rule is applied to equally spaced nodes in φ, with $2L_c+1$ points. If the function being integrated has a spherical harmonic expansion with coefficients equal to zero for degrees higher than L_c, then the quadrature yields the exact result, assuming that there are not other sources of error [31]. Moreover, quadrature in φ can be computed using the fast Fourier transform.

Remark 3.6. One would expect L_c to be greater than p and l in (3.7). Yet, without further analysis, it is not known whether a polynomial of degree L_c is a good approximation for $SL_{0j}(Y_{l,m,j})Y_{p,q,i}$, $DL_{0j}(Y_{l,m,j})Y_{p,q,i}$, $\nabla SL_{0j}(Y_{l,m,j})\cdot\widehat{\mathbf{n}}_{0i}\, Y_{p,q,i}$, and $\nabla SL_{0j}(Y_{l,m,j})\cdot\widehat{\mathbf{n}}_{0i}\, Y_{p,q,i}$, since, as the translation theorems for spherical harmonics highlight, the translation of only one spherical harmonic is expressed as another infinite series of spherical harmonics. Also, notice that (3.7) can also be computed using a translation theorem for real spherical harmonics as in [1]. In this case, the integral has an explicit expression and does not need to be computed numerically. Instead, the computing efforts focus on calculating the coefficients given by the translation theorem.

COROLLARY 3.7. *The following holds:*

$$\begin{aligned}
\left(V^0_{i,j}\left(Y_{l,m,j}\right);Y_{p,q,i}\right)_{L^2(\Gamma_i)} &= \left(V^0_{j,i}\left(Y_{p,q,i}\right);Y_{l,m,j}\right)_{L^2(\Gamma_j)},\\
\left(K^0_{i,j}\left(Y_{l,m,j}\right);Y_{p,q,i}\right)_{L^2(\Gamma_i)} &= -\frac{l}{R_j}\left(V^0_{i,j}\left(Y_{l,m,j}\right);Y_{p,q,i}\right)_{L^2(\Gamma_i)},\\
\left(K^{*0}_{j,i}\left(Y_{p,q,i}\right);Y_{l,m,j}\right)_{L^2(\Gamma_j)} &= \left(K^0_{i,j}\left(Y_{l,m,j}\right);Y_{p,q,i}\right)_{L^2(\Gamma_i)},\\
\left(W^0_{i,j}\left(Y_{l,m,j}\right);Y_{p,q,i}\right)_{L^2(\Gamma_i)} &= \frac{l}{R_j}\left(K^{*0}_{i,j}\left(Y_{l,m,j}\right);Y_{p,q,i}\right)_{L^2(\Gamma_i)}.
\end{aligned}$$

Proof. The result follows from Theorem 3.3 and the orthonormality of spherical harmonics, along with the definition of the BIOs. ∎

This last corollary allows all cross-interaction integrals between spheres i and j (3.7) to be derived from expression (3.7a), thereby saving computational effort.

3.3. Fully discrete scheme. Following section 3.1, we state the multistep semi-implicit in time and space numerical discretization of Problem 2.6.

PROBLEM 3.8. *Let* $\mathbf{v}^{L,(0)}$ *and* $\mathbf{Z}^{L,(0)}$ *in* $\mathbb{Y}_L$ *be given. Then, for* $s\in\{2,\dots,S-1\}$, *we seek* $\mathbf{v}^{L,(s)}$, $\mathbf{Z}^{L,(s)}$ *in* $\mathbb{Y}_L$ *such that*

(3.8)
$$\left(\mathbf{C_m}\overline{\partial}\mathbf{v}^{L,(s)}+\mathcal{J}_{\mathcal{N}}\left(\overline{\mathbf{v}}^{L,(s+\frac{1}{2})}\right)+\mathbf{I}^{ep}\left(\hat{\mathbf{v}}^{L,(s+\frac{1}{2})},\hat{\mathbf{Z}}^{L,(s+\frac{1}{2})}\right)+\Phi\left(\phi_e^{(s+\frac{1}{2})}\right),\mathbf{y}\right)_{\mathbb{Y}_L}=0,$$

$$\overline{\partial}^{(s)}Z_j^L=\max\left(\frac{\beta_j(\widehat{v}_j^{L,(s+\frac{1}{2})})-\widehat{Z}_j^{L,(s+\frac{1}{2})}}{\tau_{ep,j}},\frac{\beta_j(\widehat{v}_j^{L,(s+\frac{1}{2})})-\widehat{Z}_j^{L,(s+\frac{1}{2})}}{\tau_{res,j}}\right) \tag{3.9}$$

for all $\mathbf{y}\in\mathbb{Y}_L$. *For* $s=1$ *we use the equivalent weak formulation of the corrector-predictor algorithm presented in section* 3.1.

In order to solve Problem 3.8, at each time step, with the exception of the predictor-corrector algorithm, we solve the weak linear system equivalent to

(3.10)
$$\begin{bmatrix} 4\mathbf{A}_{0,\mathcal{N}} & -2\,\mathbf{X}_{\mathcal{N}}^{-1} & \mathbf{I}_{2\mathcal{N}\times\mathcal{N}}\\ -2\,\mathbf{X}_{\mathcal{N}} & 4\mathbf{A}_{1,\mathcal{N}} & -\mathbf{X}_{\mathcal{N}}\mathbf{I}_{2\mathcal{N}\times\mathcal{N}}\\ & \boldsymbol{\sigma}_{\mathcal{N}\times 4\mathcal{N}} & \frac{1}{\tau}\mathbf{C_m}\end{bmatrix}\begin{pmatrix}\overline{\mathbf{u}}_{D,0}^{L,(s+1/2)}\\ \overline{\mathbf{u}}_{N,0}^{L,(s+1/2)}\\ \overline{\mathbf{u}}_{D}^{L,(s+1/2)}\\ \overline{\mathbf{u}}_{N}^{L,(s+1/2)}\\ \mathbf{v}^{L,(s+1)}\end{pmatrix}=\begin{pmatrix}-\left(2\boldsymbol{\gamma}^0_{\phi_e^{L,(s+\frac{1}{2})}}+\mathbf{I}_{2\mathcal{N}\times\mathcal{N}}\mathbf{v}^{L,(s)}\right)\\ \mathbf{X}_{\mathcal{N}}\left(2\boldsymbol{\gamma}^0_{\phi_e^{L,(s+\frac{1}{2})}}+\mathbf{I}_{2\mathcal{N}\times\mathcal{N}}\mathbf{v}^{L,(s)}\right)\\ \frac{1}{\tau}\mathbf{C_m}\mathbf{v}^{L,(s)}-\mathbf{I}^{ep}\left(\hat{\mathbf{v}}^{L,(s+\frac{1}{2})},\hat{\mathbf{Z}}^{L,(s+\frac{1}{2})}\right)\end{pmatrix},$$

where the test function is in $\mathbb{Y}_L \times \mathbb{Y}_L \times \mathbb{Y}_L \times \mathbb{Y}_L \times \mathbb{Y}_L$. Notice that we obtain mid-steps $(s+1/2)$ for traces of extra- and intracellular potentials, whereas only the transmembrane potential is obtained at time steps s.

Remark 3.9. With the exception of the scalar operators inside of $\mathbf{A}_{0,\mathcal{N}}$ and $\mathbf{I}^{ep}$, which are computed numerically, all other matrices are diagonalizable and analytic for the geometry considered here (Corollary 3.5). Thus, the discrete matrix used to solve at each time step is almost entirely block diagonal. Note that changing $\mathbf{I}^{ep}$ without modifying the dynamics for the transmembrane potentials leads to a modified right-hand side in the linear system of (3.10).

Remark 3.10. The time step needs to be bounded by the smallest characteristic time of the system to ensure stability. In the work [11], the bound is independent of the spatial discretization but depends on the parameters of the nonlinear problem. Moreover, given the poor regularity of functions Z_j, we cannot guarantee high-order convergence in time. Yet, the use of spherical harmonics in space greatly reduces the overall number of degrees of freedom and leads to better convergence rates than first-order boundary element discretizations [28].

4. Numerical results.

In this section, we verify and test the proposed computational scheme. To this end, we first check the MTF implementation for single and multiple cells to then combine it with the multistep semi-implicit time-domain method. Next, we perform tests for linear and nonlinear dynamics. Physical parameters used throughout are given in [22, Table 1] and [17, Table 1].

4.1. Hardware and code implementation.

Numerical results were obtained in a machine with Quad Core Intel Core i7-4770, 1498MHz, 31,982.1 MiB RAM (90% available for computations), with operating system Linux Mint 20.3 Una and Kernel: 5.4.0-131-generic x86_64. Simulation codes were programmed on Python 3.10. Its installation was achieved via the open-source platform Anaconda,[5] Conda[6] 4.13.0, and using the conda-forge repository.[7] With the `numpy` library, we take advantage of vectorized computations. Moreover, we only use direct solvers, without any parallelization or matrix compression, which of course can be performed.

4.2. Code validation.

In order to validate our code, we check that computed solutions fulfill discrete Calderón identities at the boundaries as well as discrete jump conditions. Being approximations, these properties do not hold exactly; thus we define the following errors:

- Discrete Calderón exterior and interior errors, respectively:

$$\left\| (2\mathbf{A}_{0,\mathcal{N}} - \mathbf{I}) \begin{pmatrix} \mathbf{u}_{D,0}^{L,(s+1)} \\ \mathbf{u}_{N,0}^{L,(s+1)} \end{pmatrix} \right\|_{\mathbb{Y}_L \times \mathbb{Y}_L}, \left\| (2\mathbf{A}_{1,\mathcal{N}} - \mathbf{I}) \begin{pmatrix} \mathbf{u}_{D}^{L,(s+1)} \\ \mathbf{u}_{N}^{L,(s+1)} \end{pmatrix} \right\|_{\mathbb{Y}_L \times \mathbb{Y}_L}. \tag{4.1}$$

- Jump error:

$$\left\| \begin{pmatrix} \mathbf{u}_{D,0}^{L,(s+1)} \\ \mathbf{u}_{N,0}^{L,(s+1)} \end{pmatrix} - \mathbf{X}_{\mathcal{N}}^{-1} \begin{pmatrix} \mathbf{u}_{D}^{L,(s+1)} \\ \mathbf{u}_{N}^{L,(s+1)} \end{pmatrix} + \mathbf{I}_{2\mathcal{N}\times\mathcal{N}} \mathbf{v}^L + \boldsymbol{\gamma}^{0j} \phi_e^L \right\|_{\mathbb{Y}_L \times \mathbb{Y}_L} \approx 0. \tag{4.2}$$

[5] https://www.anaconda.com/products/distribution

[6] https://docs.conda.io/projects/conda/en/stable/

[7] The following packages were installed explicitly: `pyshtools` 4.10 [31] (conda install pyshtools = 4.10), `numpy` 1.23.1, `scipy` 1.9.0, and `matplotlib-base` 3.5.2.

Here the norm $\|\cdot\|_{\mathbb{Y}_L\times\mathbb{Y}_L}$ is computed as

$$\left\|\begin{pmatrix}\mathbf{u}_D^{L,(s+1)}\\ \mathbf{u}_N^{L,(s+1)}\end{pmatrix}\right\|^2_{\mathbb{Y}_L\times\mathbb{Y}_L} = \left\|\mathbf{u}_D^{L,(s+1)}\right\|^2_{\mathbb{Y}_L} + \left\|\mathbf{u}_N^{L,(s+1)}\right\|^2_{\mathbb{Y}_L}.$$

In what follows, we will use the following notation:

- Relative error in $L^2(\Gamma_j)$:

$$re_2(\phi_1,\phi_2)_j := \frac{\|\phi_1-\phi_2\|_{L^2(\Gamma_j)}}{\|\phi_1\|_{L^2(\Gamma_j)}}. \tag{4.3}$$

  This error is computed for spherical harmonics expansions when possible (3.4) or using the numerical quadrature presented at the end of section 3.2.2.
- Relative error in $C^0\left((0,T),L^2(\Gamma_1)\right)$:

$$re_{\infty,2}(\phi_1,\phi_2)_j := \frac{\max_{t_s\in T_s}\|\phi_1(t_s+\tau/2)-\phi_2(t_s+\tau/2)\|_{L^2(\Gamma_j)}}{\max_{t_s\in T_s}\|\phi_1(t_s+\tau/2)\|_{L^2(\Gamma_j)}}. \tag{4.4}$$

- Relative error in $L^2\left((0,T),L^2(\Gamma_1)\right)$:

$$re_{2,2}(\phi_1,\phi_2)_j := \frac{\|\phi_1-\phi_2\|_{L^2((0,T),L^2(\Gamma_1))}}{\|\phi_1\|_{L^2((0,T),L^2(\Gamma_1))}}. \tag{4.5}$$

  The approximation of the time integral is done by a composite trapezoidal rule using the points of the computed time mid-steps.

4.2.1. MTF validation. We verify first the MTF method without time evolution, by solving (2.10) for four different geometrical configurations and sources. In all four experiments, we set $\mathbf{v} = \mathbf{0}$ and use the point source function $\phi_e = 1/(4\pi\sigma_0\|\mathbf{r}-\mathbf{p_0}\|_2)$ as the external applied potential.

- *Example* 1: One sphere centered at the origin with intracellular conductivity σ_1 different from σ_0.
- *Example* 2: Three (aligned) spheres. The first and the third have conductivity σ_0 (phantom spheres), while the one in the middle has a different conductivity σ_1.

The parameters used for validation for Examples 1 and 2 for a single sphere are presented in Table 1, and additional parameters for Example 2 are presented in Table 2. In Example 1, the sphere has a different conductivity from that of the extracellular space, and an analytic solution can be obtained. In Figure 2 the relative errors in $L^2(\Gamma_1)$ (4.3) of the computed solutions for different L against the analytic

TABLE 1
Parameters used in section 4.2.1 *for Examples* 1 *and* 2 *for the MTF validation. Conductivity values are from* [17, *Table* 1]*, and cell radius is from* [22, *Table* 1].

Parameter	Symbol	Example 1	Unit
Intensity	a	1	μA
Source position	$\mathbf{p_0}$	(0, 0, 20)	μm
Extracellular conductivity	σ_0	5	μS/μm
Intracellular conductivity	σ_1	0.455	μS/μm
Cell radius	R_1	10	μm
Maximum degree of spherical harmonics	L	50	

TABLE 2
Parameters used for the MTF verification with $\phi_e = 1/(4\pi\sigma_0\|\mathbf{r}-\mathbf{p_0}\|_2)$ *in Example* 2*, section* 4.2.1*. Conductivities are given in* [17*, Table* 1]*, and radii are in* [22*, Table* 1].

Parameter	Symbol	Value	Unit
Cell 1 intracellular conductivity	σ_1	0.455	μS/μm
Cell 2 and 3 intracellular conductivity	σ_2, σ_3	5	μS/μm
Cell 1 radius	R_1	10	μm
Cell 2 radius	R_2	8	μm
Cell 3 radius	R_3	9	μm
Cell 1 center position	$\mathbf{p_1}$	(0, 0, 0)	μm
Cell 2 center position	$\mathbf{p_2}$	(25, 0, 0)	μm
Cell 3 center position	$\mathbf{p_3}$	(-24, 0, 0)	μm
Maximum degree of spherical harmonics	L	50	
Quadrature degree	L_c	100	

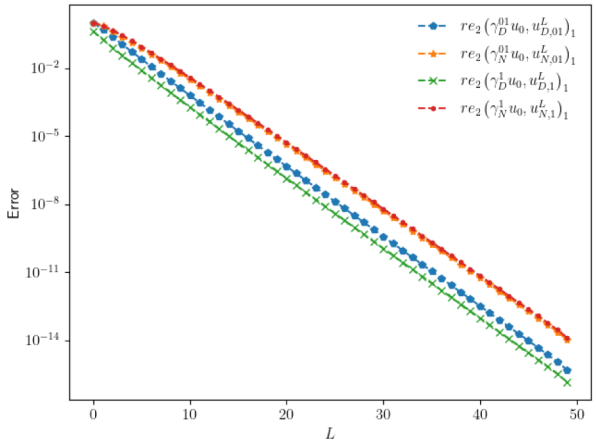

FIG. 2. *Error convergence for traces in Example* 1 *(section* 4.2.1*). The relative error* $L^2(\Gamma_1)$ (4.3) *is computed against the analytic solution with parameter values in Table* 1.

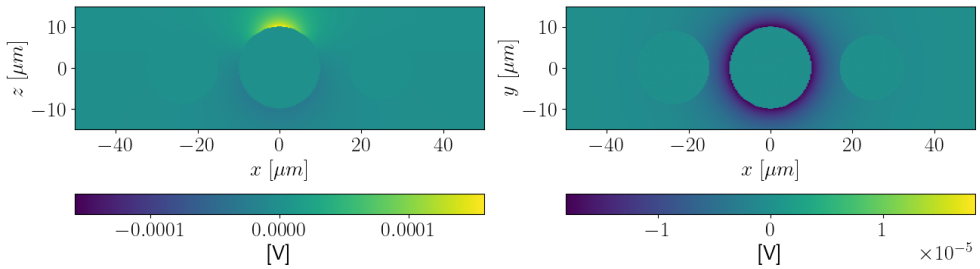

(a) Plane $y = 0$. (b) Plane $z = 0$.

FIG. 3. *Field* u_0^{50} *of Example* 2 *(section* 4.2.1*) with parameters from Table* 2.

solution are presented. The image shows the expected exponential convergence with respect to the maximum degree of the spectral basis L. Example 2 involves three spheres, two of which have the same properties as the external medium, while the one in the middle is different (see Figure 3). Therefore, the traces of the latter should be equal to the ones computed without the first two, i.e., the same as in Example 1. The relative $L^2(\Gamma_1)$ error of the difference between the analytic solution for the four

traces and the numerical one corresponding to the sphere with different conductivity is $6.06 \cdot 10^{-15}$. In Figure 3, u_0^{50} is plotted where the only sphere showing a response to ϕ_e is the sphere in the middle that has different properties compared to the external medium. Discrete Calderón and jump errors are of order 10^{-16} considered as zero.

4.2.2. Multistep semi-implicit time approximation validation: Linear case. We validate the proposed time scheme by solving problem (3.8) for a linear current with only one cell,

$$c_{m,1}\partial_t v_1 + \frac{1}{r_{m,1}} v_j = -\sigma_1 \gamma_N^1 u_1,$$

where instead of $I_1^{ep}(v_1, Z_1)$ we use $r_{m,1}^{-1} v_j$. Additionally, we assume that ϕ_e can be factorized as $\phi_e(t, \mathbf{r}) = \phi_{time}(t)\phi_{space}(\mathbf{r})$. If ϕ_{space} is expanded in spherical harmonics, the coefficients for the equivalent expansion of v_1, denoted by $v_1^{l,m}$, can be obtained by solving

$$\partial_t v_1^{l,m} + \alpha_1^{l,m}\ v_1^{l,m} = -\beta_1^{l,m}\ \phi_{time}(t),$$

with

$$\alpha_1^{l,m} := \frac{1}{c_m R_m} + \frac{\sigma_0\sigma_1 l(l+1)}{c_m R_1(\sigma_0(l+1) + \sigma_1 l)}, \quad \beta_1^{l,m} := \frac{\sigma_0\sigma_1 l(b_{d,l,m}(l+1) - b_{n,l,m}R_1)}{c_m R_1(\sigma_0(l+1) + \sigma_1 l)},$$

where $b_{d,l,m}$ and $b_{n,l,m}$ are the coefficients of degree l and order m for the Dirichlet and Neumann trace expansions of ϕ_{space} on the cell's membrane, respectively. Then, the spherical harmonic expansion coefficients of v_1 are

$$v_1^{l,m}(t) = -\beta_1^{l,m} e^{-\alpha_1^{l,m}t} \int_0^t \phi_{time}(s) e^{\alpha_1^{l,m}s} ds + v_1^{l,m}(0) e^{-\alpha_1^{l,m}t}.$$

We present simulation results for two different time behaviors for ϕ_e, $\phi_{time-exp} = e^{-t}$, and $\phi_{time-cte} = 1$. We use a point source function for the spatial part of ϕ_e. Parameters are presented in Table 3. In Figure 4, the absolute error of the difference between $\overline{v}_1^{23}$ (for $\tau = 2.5 \cdot 10^{-2}\mu$s) and v_1 in space is presented for each time mid-step. We compute also $\frac{\tau^2}{4} \left\| \partial_t^2 v_1 \right\|_{L^2(\Gamma_j)}$ to validate the first bound in Theorem 3.2. For $\phi_{time-exp}$, the absolute error satisfies the first bound in Theorem 3.2 everywhere except for the

TABLE 3

Parameters used for the time scheme validation in section 4.2.2 *where linear dynamics are assumed. The external potential is* $\phi_e = I(t)/(4\pi\sigma_0\|\mathbf{r} - \mathbf{p_0}\|_2)$, *and only one cell is considered. Conductivity values are given in* [17, *Table* 1], *the cell radius and the specific membrane capacitance are given in* [22, *Table* 1], *and the specific membrane resistance is from* [12, *Table* 1].

Parameter	Symbol	Values	Unit
Intensity	$I(t)$	e^{-t} and 1	μA
Source position	$\mathbf{p_0}$	(0, 0, 50)	μm
Extracellular conductivity	σ_0	5.00	μS/μm
Intracellular conductivity	σ_1	$4.55 \cdot 10^{-1}$	μS/μm
Specific membrane capacitance	$c_{m,1}$	$9.50 \cdot 10^{-3}$	pF/(μm)^2 (=F/m^2)
Specific membrane resistance	$r_{m,1}$	$1.00 \cdot 10^5$	MΩ(μm)^2
Cell radius	R_1	7.00	μm
Length time step	τ	$2.50 \cdot 10^{-2}$	μs
Final time	T	2.50	μs
Maximum degree of spherical harmonics	L	25	

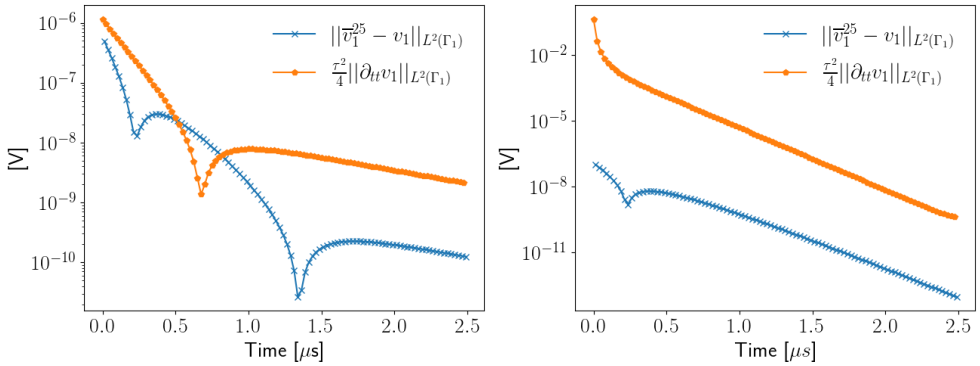

(a) $\phi_{time-ext}(t) = e^{-t}$. (b) $\phi_{time-cte}(t) = 1$.

FIG. 4. *Absolute error in $L^2(\Gamma_1)$ between $\overline{v}_1^{25}$ (discrete approximation) and v_1 (analytic solution), as well as $\frac{\tau^2}{4}\|\partial_t^2 v_1(t)\|_{L^2(\Gamma_j)}$, plotted to verify the bound given by Theorem 3.2 for the time scheme from section 4.2.2 where linear dynamics are assumed. The time step τ is $2.5 \cdot 10^{-2}$ μs, and the rest of the parameters used are in Table 3.*

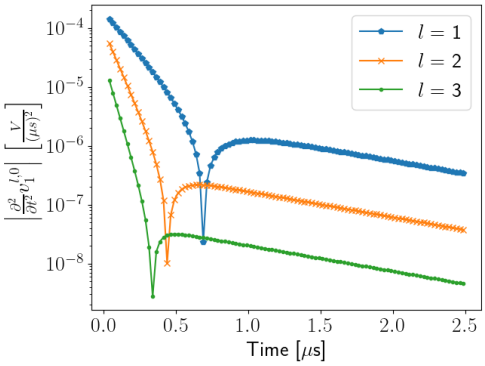

FIG. 5. *Absolute values of the analytically obtained second derivatives for the three most significant coefficients for the linear dynamics example from section 4.2.2 with $\phi_{time-ext}(t) = e^{-t}$. It can be seen that the dip for $l = 1$ matches the dip from Figure 4(a).*

range between 0.4 μs and 0.7 μs, where a dip in $\frac{\tau^2}{4}\|\partial_t^2 v_1(t)\|_{L^2(\Gamma_j)}$ occurs. This is due to the second derivative of the most significant term ($l = 1$) approaching zero (see Figure 5). In contrast, for $\phi_{time-cte}$ the bound is fulfilled at all times.

Finally, Figure 6 presents the relative error in time and space for decreasing values of τ. We compute the error using two norms: an approximation of the $C^0\left((0,T), L^2(\Gamma_1)\right)$-norm taking the maximum value at mid-steps (4.4), and an approximation of the $L^2\left((0,T), L^2(\Gamma_1)\right)$-norm, using a composite trapezoidal rule evaluated at the computed mid-steps (4.5). We observe that the slope of the errors in the log-log plot is close to two, therefore the error decreases as τ^2.

4.3. Numerical results for a single cell with nonlinear dynamics. After having verified our numerical scheme for the linear dynamics, we now study the nonlinear dynamics for a single cell (Problem 2.6). Note that in [11, Theorem 6.14] error estimates are given in two dimensions for the Hodgkin–Huxley model. The estimates depend on four terms. The first two are the norms of the difference between initial conditions and approximated ones used in the computations. The third error term is

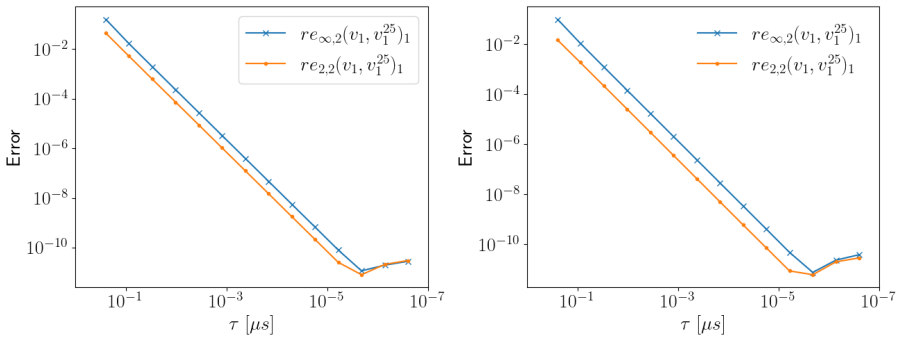

(a) $\phi_{time-exp}(t) = e^{-t}$. (b) $\phi_{time-cte}(t) = 1$.

FIG. 6. *Error convergence for diminishing time steps τ for the time scheme in section* 4.2.2 *where linear dynamics are assumed. Slopes on the log-log plot show error converges as τ^2. Relative errors $re_{\infty,2}(v_1, v_1^{25})_1$ and $re_{2,2}(v_1, v_1^{25})_1$ are given in* (4.4) *and* (4.5)*, respectively. Simulation parameters can be found in Table* 3.

TABLE 4

Parameters used for the simulation of a single cell with nonlinear dynamics (2.2e) *in section* 4.3.1 *when studying the time convergence with fixed L. Parameters used are found in* [17, *Table* 1].

Parameter	Symbol	Values	Unit
Cell radius	R_1	$1.00 \cdot 10^1$	μm
Time part of ϕ_e	ϕ_{time}	1.00	
Spatial part of ϕ_e	$\phi_{spatial}$	$5\ z \cdot 10^{-2}$	V
Extracellular conductivity	σ_0	5.00	μS/μm
Intracellular conductivity	σ_1	$4.55 \cdot 10^{-1}$	μS/μm
Lipid surface conductivity	$S_{L,1}$	$1.90 \cdot 10^{-6}$	μS/(μm)^2
Irreversible surface conductivity	$S_{ir,1}$	$2.50 \cdot 10^2$	μS/(μm)^2
Specific membrane capacitance	$c_{m,1}$	$9.50 \cdot 10^{-3}$	pF/(μm)^2
Transmembrane potential threshold	$V_{rev,1}$	1.50	V
Electropermeabilization switch speed	$k_{ep,1}$	$4.00 \cdot 10^1$	V^{-1}
Characteristic time of electropermeabilization	$\tau_{ep,1}$	1.00	μs
Characteristic resealing time	$\tau_{res,1}$	$1.00 \cdot 10^3$	μs
Final time	T	$2.60 \cdot 10^1$	μs
Maximum degree of spherical harmonics	L	1	
Quadrature degree	L_c	2	

related to the spatial discretization, where a spectral basis in two dimensions is used, and this term is proved to decay exponentially with the total number of functions in the spatial discretization basis. Finally, the fourth error term is due to the time approximation, converging as τ^2. Here, we expect a similar behavior. In other words, fixing the maximum degree of spherical harmonics L used in the space discretization and decreasing the length of the time step τ, we expect to see the error converging to a constant depending on L. Similarly, if we fix τ and increase L, we expect the error to converge to a constant depending on τ.

4.3.1. Time convergence for a fixed L. We use the parameters presented in Table 4 to solve the nonlinear discrete Problem 3.8, with external applied potential $\phi_e = 5z \cdot 10^{-2}$ and initial conditions equal to zero. Since we no longer possess an analytic solution for comparison, we check for convergence as time steps become smaller. We remark that L is fixed, and we use $L = 1$, along with $L_c = 2$.

Table 5 displays the error norms between two successively refined solutions for different time steps. These results show a linear convergence rate as the time step

TABLE 5
Error convergence for the nonlinear problem with one cell from section 4.3.1 for fixed L. Computed norms are the difference between two successive solutions. Parameters used are in Table 4.

τ_i	Value [μs]	$\max_{t\in[0,T]} \left\|v_1^{1,\tau_{i+1}} - v_1^{1,\tau_i}\right\|_{L^2(\Gamma_1)}$	$\max_{t\in[0,T]} \left\|Z_1^{1,\tau_{i+1}} - Z_1^{1,\tau_i}\right\|_{L^2(\Gamma_1)}$
τ_1	$2.6\cdot10^{-3}$	–	–
τ_2	$2.6\cdot10^{-4}$	$8.8\cdot10^{0}$	$4.64\cdot10^{-3}$
τ_3	$2.6\cdot10^{-5}$	$9.0\cdot10^{-1}$	$3.02\cdot10^{-4}$
τ_4	$2.6\cdot10^{-6}$	$9.7\cdot10^{-2}$	$3.59\cdot10^{-5}$
τ_5	$2.6\cdot10^{-7}$	$9.7\cdot10^{-9}$	$3.15\cdot10^{-6}$

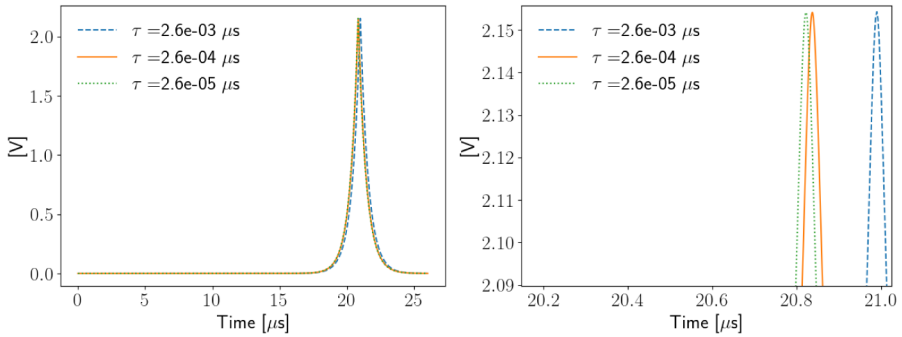

FIG. 7. *Evolution of v_1^1 at the north pole of the cell ($\theta = 0$) for different lengths of time step τ illustrating the time convergence for fixed L, section 4.3.1. The image at the right is zoomed near to the maximum value of v_1^1. Parameters employed are given in Table 4.*

decreases, and thus we do not obtain the same convergence rate reported in [11]. This is due to the lesser regularity in time of the solutions; Z_1 is not twice differentiable, as can be noticed from (2.4). In Figure 7, we plot the evolution of the transmembrane potential v_1^1 for three different values of τ. Though the solution shapes are similar, peaks appear at different locations and coincide as the time step decreases. Specifically, between $\tau = 2.6\cdot10^{-3}\mu$s and $\tau = 2.6\cdot10^{-4}\mu$s, there is a delay of less than $1.6\cdot10^{-1}$ μs, while between $\tau = 2.6\cdot10^{-4}\mu$s and $\tau = 2.6\cdot10^{-5}\mu$s, the delay is less than $1.7\cdot10^{-2}$ μs.

4.3.2. Spatial convergence with nonlinear dynamics. We now present numerical results for different maximum degrees of the spherical harmonics, $L = 51$ and $L \in [1, 2, \ldots, 36]$, computed with $L_c = 150$. Given that we use a spectral discretization in space, we expect an exponential decrease in the error when increasing the maximum degree[8] L—recall that the number of spatial discretization functions basis is $(L+1)^2$. The external applied potential is $\phi_e = 5z\cdot10^{-2}$ until $t = 5$ and equal to zero thereafter. Initial conditions are set to zero, and the length of the time step used is $\tau \approx 2.4\cdot10^{-3}$.

We compute the relative errors between v_1^L and v_1^{51} and between Z_1^L and Z_1^{51}. The results are shown in Figure 8. The plots are in a log-linear scale, and the errors tends to form a straight line with the slope of order 10^{-2}, which suggests an exponential rate of convergence. Recall that in our case β (cf. (2.1)) is only C^0-continuous due to the discontinuity of the derivative at the origin and Z_1 is only twice differentiable in time

[8]The parameters used are provided in Table 6. Notice that extra- and intracellular conductivities have different values from the previous simulations, and were changed to obtain a response of the impulse sooner.

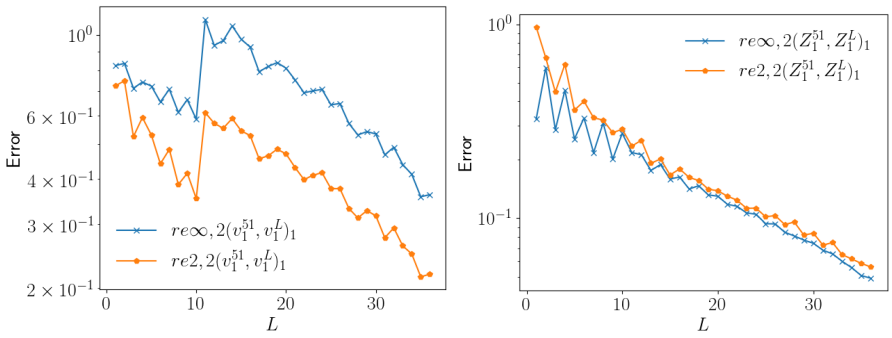

(a) Relative norms for v_1^L. (b) Relative norms for Z_1^L.

FIG. 8. *Spatial convergence for the nonlinear dynamics of section* 4.3.2. *Relative norms are computed against an overkill of* $L = 51$. *On the left are results for* v_1^L, *while on the right* Z_1^L *is displayed with time step* $\tau \approx 2.4 \cdot 10^{-2}$ μs. *The* x*-axis indicates the maximum degree used for discretization. Convergence starts from* $L = 11$. *Plots are in log-linear scale, and error tends to form a straight line with slope of approximately* -10^{-2}, *i.e., exponential convergence. Parameters are given in Table* 6. *The expressions for the relative errors* $re_{\infty,2}(v_1^{51},v_1^L)_1$ *and* $re_{2,2}(v_1^{51},v_1^L)_1$ *are given in* (4.4) *and* (4.5), *respectively.*

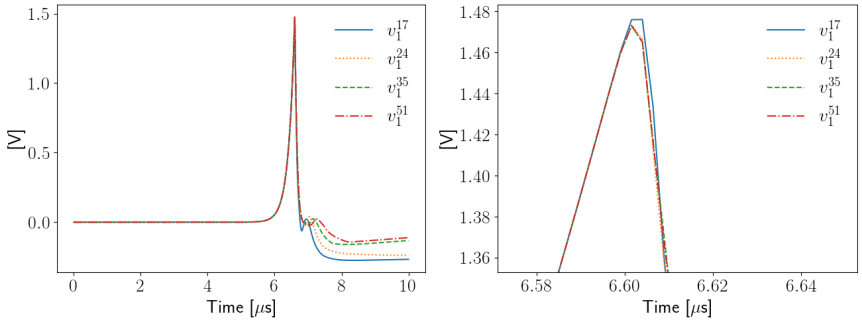

(a) Transmembrane potentials (b) Zoom at peak.

FIG. 9. *Evolution of the transmembrane potentials* v_1^{17}, v_1^{24}, v_1^{35}, *and* v_1^{51} *at the north pole of the cell* ($\theta = 0$) *obtained in section* 4.3.2 *where the spatial convergence for one cell in the nonlinear case is studied. The time step used is* $\tau \approx 2.4 \cdot 10^{-2}$ μs, *with parameters given in Table* 6.

(2.4), worsening the rate of convergence. However, as shown in [28], the numerical method presented should converge faster than a first-order boundary element method and twice as fast with respect to the number of functions used to construct the approximation in the worst case. While the obtained Z_1 is an even function in space, v_1 is an odd one. Thus, the nonlinear current is an odd function in space. Since the external applied potential is an odd function, we expect v_1 to have an odd component, while Z_1 is defined by an ordinary differential equation that takes v_1 into an even function. Finally, in Figure 9 we plot the evolution in time of v_1^{17}, v_1^{24}, v_1^{35}, and v_1^{51} at the north pole. The differences between the results are more noticeable after the peak of the potential and when the cell tries to stabilize it.

4.4. Results with multiple cells. In previous sections, the convergence of the numerical method was studied for a single cell. We proceed now with the case of multiple cells to perform five experiments in the nonlinear case. The examples presented highlight how the distance among cells affects the results as all cell conductivities are set to the same value σ_1.

TABLE 6

Parameters used in the numerical simulations in sections 4.3.2 *and* 4.4*, with the nonlinear dynamics of the electropermeabilization model. The specific choice of extra- and intracellular conductivities, different from the previous simulations, allows us to obtain a response of the impulse sooner in time. The rest of the parameters are from* [17*, Table* 1]*. The external applied potential used is equal to zero after* $t = 5$ μs*.*

Parameter	Symbol	Values	Unit
Cell radius	R_1	$1.00 \cdot 10^1$	μm
External applied potential	ϕ_e	$5\ z \cdot 10^{-2}$	V
Extracellular conductivity	σ_0	$1.50 \cdot 10^1$	μS/μm
Intracellular conductivity	σ_1	1.50	μS/μm
Specific membrane capacitance	$c_{m,1}$	$9.50 \cdot 10^{-3}$	pF/(μm)^2 (=F/m^2)
Lipid surface conductivity	$S_{L,1}$	$1.90 \cdot 10^{-6}$	μS/(μm)^2
Irreversible surface conductivity	$S_{ir,1}$	$2.50 \cdot 10^2$	μS/(μm)^2
Transmembrane potential threshold	$V_{rev,1}$	1.50	V
Electropermeabilization switch speed	$k_{ep,1}$	$4.00 \cdot 10^1$	V^{-1}
Characteristic time of electropermeabilization	$\tau_{ep,1}$	1.00	μs
Characteristic resealing time	$\tau_{res,1}$	$1.00 \cdot 10^3$	μs
Final time	T	$1.00 \cdot 10^1$	μs

TABLE 7

Center positions for Examples 3 *and* 4 *from section* 4.4*, where nonlinear dynamics are simulated.*

Center position	Symbol	Example 3	Example 4	Unit
Cell 1	$\mathbf{p_1}$	(0, 0, 0)	(0, 0, 0)	μm
Cell 2	$\mathbf{p_2}$	(200, 0, 0)	(25, 0, 0)	μm
Cell 3	$\mathbf{p_3}$	(-200, 0, 0)	(-25, 0, 0)	μm

TABLE 8

Positions of cells in Example 5 *from section* 4.4*, where nonlinear dynamics are simulated.*

Center position	Symbol	Value in μm	Center position	Symbol	Value in μm
Cell 1	$\mathbf{p_1}$	(0, 0, 0)	Cell 5	$\mathbf{p_5}$	(0, 0, 25)
Cell 2	$\mathbf{p_2}$	(25, 0, 0)	Cell 5	$\mathbf{p_6}$	(25, 0, 25)
Cell 3	$\mathbf{p_3}$	(0, 25, 0)	Cell 7	$\mathbf{p_7}$	(0, 25, 25)
Cell 4	$\mathbf{p_4}$	(25, 25, 0)	Cell 8	$\mathbf{p_8}$	(25, 25, 25)

- *Example* 3: Three cells aligned along the x-axis and far from each other, with distance between cells $18R_1$.
- *Example* 4: Three cells aligned along the x-axis, near to each other, with distance between cells $\frac{1}{2}R_1$.
- *Example* 5: Eight cells aligned in a cubic lattice, the nearest distance between two cells is $\frac{1}{2}R_1$, the first sphere is at the origin.

Cell radii and physical parameters used for Examples 3–5 are presented in Table 6. Extra- and intracellular conductivity values were changed so as to obtain a response sooner. Cells centers in Examples 3 and 4 are given in Table 7 and sketched in Figure 10, while those in Example 5 are located at the corners of a cube of length 25 μm (cf. Table 8). Throughout initial conditions are set to zero. The external applied potential in Examples 3–5 is $\phi_e = 5z \cdot 10^{-2}$ until $t = 5$ μs and zero thereafter.

In what follows, we present results for a time step $\tau \approx 6.1 \cdot 10^{-4}$. The maximum degree of spherical harmonics used for Examples 3 and 4 is $L = 35$, while for Example 5 we set $L = 25$. Quadrature degree used in all examples is $L_c = 100$. Figures 11, 12, and 14 showcase the evolution of the transmembrane potentials v_j^L and the variables Z_j^L for each cell at their north pole.

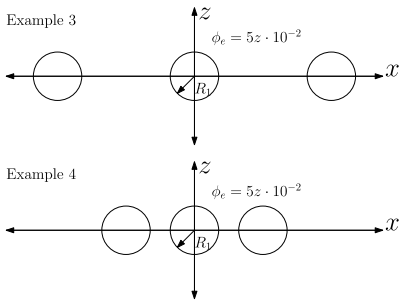

FIG. 10. *Illustration of cells positions for Examples* 3 *and* 4 *in section* 4.4.

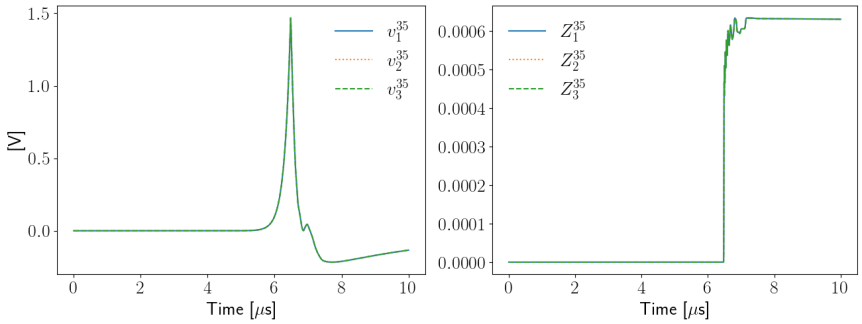

FIG. 11. *Evolution of* v_j^{35} *and* Z_j^{35} *at the north pole of each* j *cell* ($\theta = 0$)*, from Example* 3 *in section* 4.4. *The time step is* $\tau \approx 6.1 \cdot 10^{-4}$. *Parameters employed are found in Tables* 6 *and* 7.

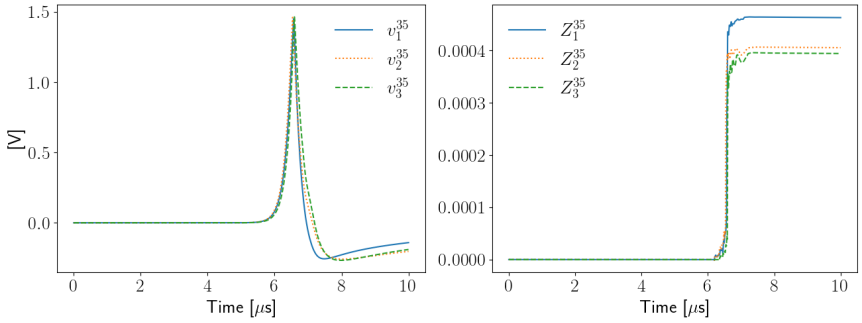

FIG. 12. *Evolution of* v_j^{35} *and* Z_j^{35} *at the north pole of each* j *cell* ($\theta = 0$)*, from Example* 4 *from section* 4.4. *Cells are near each other and the interaction among them influences the transmembrane potential* v_j^{35} *and* Z_j^{35} *(cf. Example* 3 *in contrast). The only difference between Examples* 3 *and* 4 *is the distance between successive cells. The time step is* $\tau \approx 6.1 \cdot 10^{-4}$, *and the parameters employed are given in Tables* 6 *and* 7.

In Example 3, the cells are aligned along the x-axis and $\phi_e = 5z \cdot 10^{-2}$. Therefore, the external excitation from ϕ_e is the same for the three spheres, i.e., the contribution of ϕ_e to the right-hand side is the same for each sphere. Since the cells are relatively far from each other, there is almost no interaction among them and the potentials v_j^{35} and Z_j^{35} look similar for all j (see Figure 9). In Example 4, we take the same parameters as in Example 3, but the distance between cells is reduced to $\frac{1}{2}R_1$. Hence, the interaction among cells is stronger, and, as expected, the shapes of the potentials

v_j^{35} and Z_j^{35} change (see Figure 12). One should compare these results with the previous example in Figure 11. Due to the symmetry and the form of $\phi_e = 5z \cdot 10^{-2}$, cells 2 and 3 should have the same response at the north pole. However, they are slightly different, hinting at further time step refinement. To check this, in Figure 13 we present results for a second simulation with a refined time step, between 6 μs and 8 μs, using the previous simulation at that time as initial condition. One can immediately see that the transmembrane potentials recover the stated symmetry.

Finally, in Example 5 eight cells close to each other are simulated. In Figure 14, the corresponding transmembrane voltage v_j^{25} and Z_j^{25} at the north pole are presented. The cells with the centers in the plane $z = 0$ show similar response—see Table 8 for the center position of each cell—while the cells with centers in the plane $z = 25$ have similar response, too, while differing from cells beneath them. Figure 15 shows six

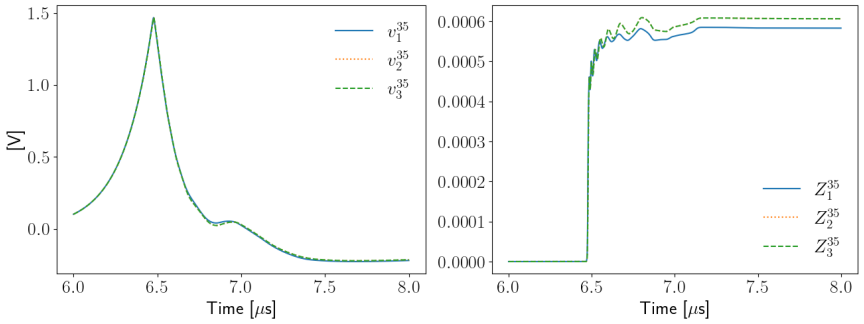

FIG. 13. *Evolution of v_j^{35} and Z_j^{35} at the north pole of each j cell ($\theta = 0$), from a simulation with a refinement in time of Example* 4 *from section* 4.4. *Cells are near each other and the interaction among them influences the transmembrane potential v_j^{35} and Z_j^{35} (cf. Example* 3 *in contrast). The only difference between Examples* 3 *and* 4 *is the distance between successive cells. The time step is $\tau \approx 4.9 \cdot 10^{-4}$.*

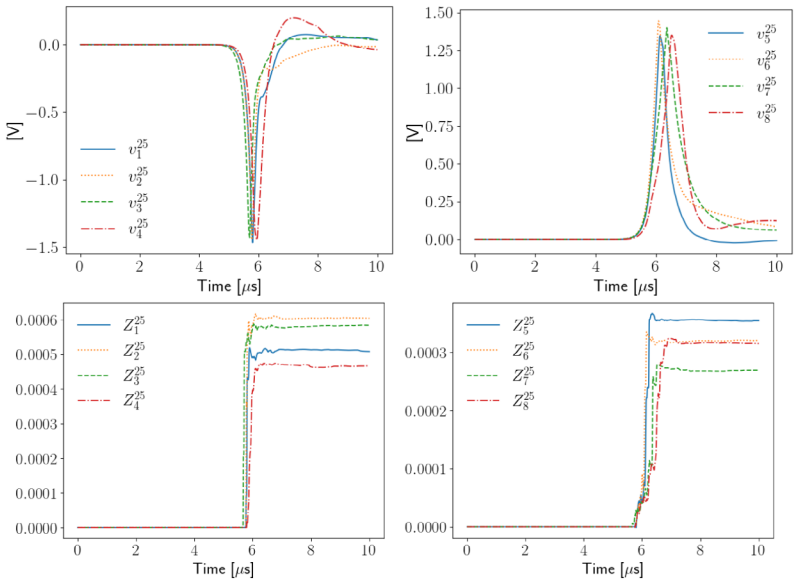

FIG. 14. *Evolution of v_j^{25} and Z_j^{25} at the north pole of each cell ($\theta = 0$), from Example* 5 *from section* 4.4. *The first four cells are in the plane $z = 0$, while the others are in the plane $z = 25$. The time step is $\tau \approx 6.1 \cdot 10^{-4} \mu s$. The rest of parameters employed are given in Tables* 6 *and* 7.

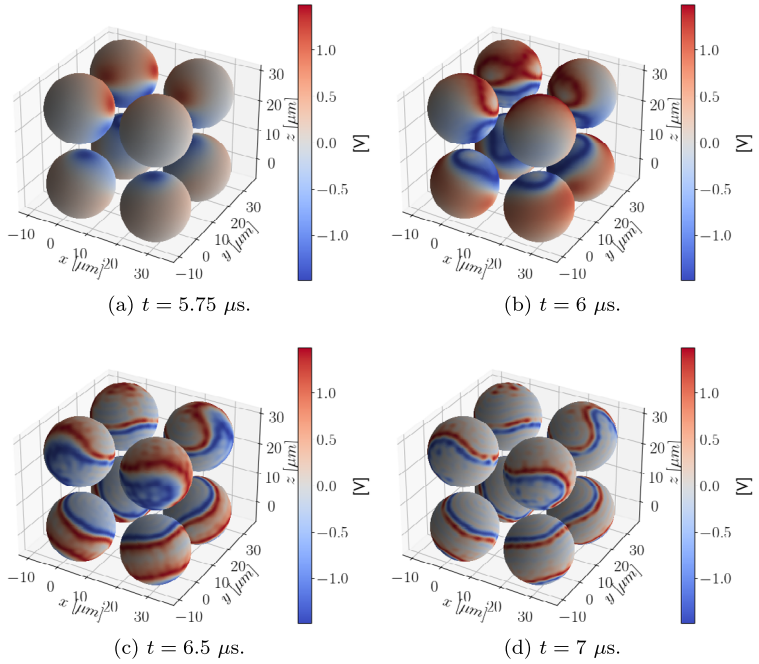

(a) $t = 5.75$ μs. (b) $t = 6$ μs.

(c) $t = 6.5$ μs. (d) $t = 7$ μs.

FIG. 15. *Transmembrane voltages* v_j^{25} *obtained in Example* 9 *of section* 4.4 *at different times. The length of the time step is* $\tau \approx 6.1 \cdot 10^{-4}$. *Parameters employed are given in Tables* 6 *and* 7.

snapshots of the transmembrane voltages for the eight cells. The transmembrane voltage starts changing earlier on parts of the surface closest to the rest of the cells.

5. Conclusions and future work. We studied the electropermeabilization of disjoint cells following the nonlinear dynamics from [17] and recast the volume boundary value problem via an MTF to obtain a parabolic system of boundary integral equations on the cell membrane. This extends significantly the numerical method presented in [11]. Still, the multistep semi-implicit time scheme though stable requires relatively small time steps with low convergence rates due to the poor regularity in time. For simplicity, we assumed spherical cells, but other shapes can be easily considered with similar spectral convergence rates in space.

The present model can be directly adapted to different dynamical models as long as this only involves changing the nonlinear term and/or variables independent of the transmembrane potential. This leads to modifying only the right-hand side of the system (3.10). Further improvements to the numerical method to be implemented in the future are matrix compression and parallelization techniques, along with an efficient solver for linear systems at each time step.

REFERENCES

[1] A. A. AGANIN AND A. I. DAVLETSHIN, *Transformation of irregular solid spherical harmonics with parallel translation of the coordinate system*, Lobachevskii J. Math., 39 (2018), pp. 433–438, https://doi.org/10.1134/S1995080218030022.

[2] H. AMMARI, T. WIDLAK, AND W. ZHANG, *Towards monitoring critical microscopic parameters for electropermeabilization*, Quart. Appl. Math., 75 (2016), pp. 1–17, https://doi.org/10.1090/qam/1449.

[3] S.-E. Choi, H. Khoo, and S. C. Hur, *Recent advances in microscale electroporation*, Chem. Rev., 122 (2022), pp. 11247–11286, https://doi.org/10.1021/acs.chemrev.1c00677.
[4] X. Claeys, R. Hiptmair, and C. Jerez-Hanckes, *Multitrace boundary integral equations*, in Direct and Inverse Problems in Wave Propagation and Applications, Radon Ser. Comput. Appl. Math. 14, De Gruyter, Berlin, 2013, pp. 51–100.
[5] X. Claeys, R. Hiptmair, C. Jerez-Hanckes, and S. Pintarelli, *Novel multitrace boundary integral equations for transmission boundary value problems*, in Unified Transform for Boundary Value Problems: Applications and Advances, A. S. Fokas and B. Pelloni, eds., SIAM, Philadelphia, 2015, pp. 227–258, https://doi.org/10.1137/1.9781611973822.ch7.
[6] D. Colton and R. Kress, *Inverse Acoustic and Electromagnetic Scattering Theory*, Appl. Math. Sci. 93, 3rd ed., Springer Science & Business Media New York, 2013.
[7] W. Freeden and M. Gutting, *Special Functions of Mathematical (Geo-)Physics*, Springer Basel, Basel, 2013.
[8] J. Gallier and J. Quaintance, *Spherical harmonics and linear representations of Lie groups*, in Differential Geometry and Lie Groups, Springer, 2020, pp. 265–360.
[9] A. Guittet, M. Lepilliez, S. Tanguy, and F. Gibou, *Solving elliptic problems with discontinuities on irregular domains—the Voronoi Interface Method*, J. Comput. Phys., 298 (2015), pp. 747–765, https://doi.org/10.1016/j.jcp.2015.06.026.
[10] A. Guittet, C. Poignard, and F. Gibou, *A Voronoi Interface approach to cell aggregate electropermeabilization*, J. Comput. Phys., 332 (2017), pp. 143–159, https://doi.org/10.1016/j.jcp.2016.11.048.
[11] F. Henríquez and C. Jerez-Hanckes, *Multiple traces formulation and semi-implicit scheme for modelling biological cells under electrical stimulation*, ESAIM Math. Model. Numer. Anal., 52 (2018), pp. 659–703, https://doi.org/10.1051/m2an/2018019.
[12] F. Henríquez, C. Jerez-Hanckes, and F. Altermatt, *Boundary integral formulation and semi-implicit scheme coupling for modeling cells under electrical stimulation*, Numer. Math., 136 (2017), pp. 101–145, https://doi.org/10.1007/s00211-016-0835-9.
[13] R. Hiptmair and C. Jerez-Hanckes, *Multiple traces boundary integral formulation for Helmholtz transmission problems*, Adv. Comput. Math., 37 (2012), pp. 39–91, https://doi.org/10.1007/s10444-011-9194-3.
[14] R. Hiptmair, C. Jerez-Hanckes, J.-F. Lee, and Z. Peng, *Domain decomposition for boundary integral equations via local multi-trace formulations*, in Domain Decomposition Methods in Science and Engineering XXI, Springer International Publishing, 2014, pp. 43–57.
[15] J. D. Jackson, *Classical Electrodynamics*, 3rd ed., student ed ed., Wiley, Hoboken, NY, 2013.
[16] C. Jerez-Hanckes, J. Pinto, and S. Tournier, *Local multiple traces formulation for high-frequency scattering problems*, J. Comput. Appl. Math., 289 (2015), pp. 306–321, https://doi.org/10.1016/j.cam.2014.12.045.
[17] O. Kavian, M. Leguèbe, C. Poignard, and L. Weynans, *"Classical" electropermeabilization modeling at the cell scale*, J. Math. Biol., 68 (2014), pp. 235–265, https://doi.org/10.1007/s00285-012-0629-3.
[18] K. Kim and W. G. Lee, *Electroporation for nanomedicine: A review*, J. Mater. Chem. B, 5 (2017), pp. 2726–2738, https://doi.org/10.1039/C7TB00038C.
[19] T. Kotnik, L. Rems, M. Tarek, and D. Miklavčič, *Membrane electroporation and electropermeabilization: Mechanisms and models*, Annu. Rev. Biophys., 48 (2019), pp. 63–91, https://doi.org/10.1146/annurev-biophys-052118-115451.
[20] M. Leguèbe, A. Silve, L. M. Mir, and C. Poignard, *Conducting and permeable states of cell membrane submitted to high voltage pulses: Mathematical and numerical studies validated by the experiments*, J. Theor. Biol., 360 (2014), pp. 83–94, https://doi.org/10.1016/j.jtbi.2014.06.027.
[21] W. C. H. McLean, *Strongly Elliptic Systems and Boundary Integral Equations*, Cambridge University Press, Cambridge, New York, 2000.
[22] P. Mistani, A. Guittet, C. Poignard, and F. Gibou, *A parallel Voronoi-based approach for mesoscale simulations of cell aggregate electropermeabilization*, J. Comput. Phys., 380 (2019), pp. 48–64, https://doi.org/10.1016/j.jcp.2018.12.009.
[23] J. C. Neu and W. Krassowska, *Asymptotic model of electroporation*, Phys. Rev. E, 59 (1999), pp. 3471–3482, https://doi.org/10.1103/PhysRevE.59.3471.
[24] E. Onemli, S. Joof, C. Aydinalp, N. Pastaci Özsobaci, F. Ateş Alkan, N. Kepil, I. Rekik, I. Akduman, and T. Yilmaz, *Classification of rat mammary carcinoma with large scale in vivo microwave measurements*, Sci. Rep., 12 (2022), 349, https://doi.org/10.1038/s41598-021-03884-7.

[25] R. Plonsey and D. B. Heppner, *Considerations of quasi-stationarity in electrophysiological systems*, Bull. Math. Biophys., 29 (1967), pp. 657–664, https://doi.org/10.1007/BF02476917.

[26] M.-P. Rols, *Electropermeabilization, a physical method for the delivery of therapeutic molecules into cells*, Biochim. Biophys. Acta, 1758 (2006), pp. 423–428, https://doi.org/10.1016/j.bbamem.2006.01.005.

[27] S. A. Sauter and C. Schwab, *Boundary Element Methods*, Springer Ser. Comput. Math. 39, Springer, Berlin, Heidelberg, 2010.

[28] E. P. Stephan and M. Suri, *On the convergence of the p-version of the boundary element Galerkin method*, Math. Comp., 52 (1989), pp. 31–48, https://doi.org/10.1090/S0025-5718-1989-0947469-5.

[29] V. Thomée, *Galerkin Finite Element Methods for Parabolic Problems*, Springer Ser. Comput. Math. 25, 2nd ed., Springer, Berlin, New York, 2006.

[30] F. Vico, L. Greengard, and Z. Gimbutas, *Boundary integral equation analysis on the sphere*, Numer. Math., 128 (2014), pp. 463–487, https://doi.org/10.1007/s00211-014-0619-z.

[31] M. A. Wieczorek and M. Meschede, *SHTools: Tools for working with spherical harmonics*, Geochem. Geophys. Geosyst., 19 (2018), pp. 2574–2592, https://doi.org/10.1029/2018GC007529.